Axisymmetric general relativistic simulations of the accretion-induced collapse of white dwarfs

E. B. Abdikamalov,[1,2,3] C. D. Ott,[4,5,6] L. Rezzolla,[3,7] L. Dessart,[8] H. Dimmelmeier,[9] A. Marek,[10] and H.-T. Janka[10]

[1]*International School for Advanced Studies (SISSA) and INFN, Trieste, Italy*
[2]*Institute of Nuclear Physics, Uzbekistan Academy of Sciences, Ulughbek, Uzbekistan*
[3]*Max-Planck-Institut für Gravitationsphysik, Albert-Einstein-Institut, Potsdam, Germany*
[4]*TAPIR, California Institute of Technology, Pasadena, California, USA*
[5]*Niels Bohr International Academy, Niels Bohr Institute, Copenhagen, Denmark*
[6]*Center for Computation and Technology, Louisiana State University, Louisiana, USA*
[7]*Department of Physics and Astronomy, Louisiana State University, Baton Rouge, Louisiana, USA*
[8]*Laboratoire d'Astrophysique de Marseille, Marseille, France*
[9]*Department of Physics, Aristotle University of Thessaloniki, Greece*
[10]*Max Planck Institute for Astrophysics, Garching, Germany*

(Received 15 October 2009; published 10 February 2010)

The accretion-induced collapse (AIC) of a white dwarf may lead to the formation of a protoneutron star and a collapse-driven supernova explosion. This process represents a path alternative to thermonuclear disruption of accreting white dwarfs in type Ia supernovae. In the AIC scenario, the supernova explosion energy is expected to be small and the resulting transient short-lived, making it hard to detect by electromagnetic means alone. Neutrino and gravitational-wave (GW) observations may provide crucial information necessary to reveal a potential AIC. Motivated by the need for systematic predictions of the GW signature of AIC, we present results from an extensive set of general-relativistic AIC simulations using a microphysical finite-temperature equation of state and an approximate treatment of deleptonization during collapse. Investigating a set of 114 progenitor models in axisymmetric rotational equilibrium, with a wide range of rotational configurations, temperatures and central densities, and resulting white dwarf masses, we extend previous Newtonian studies and find that the GW signal has a generic shape akin to what is known as a ''type III'' signal in the literature. Despite this reduction to a single type of waveform, we show that the emitted GWs carry information that can be used to constrain the progenitor and the postbounce rotation. We discuss the detectability of the emitted GWs, showing that the signal-to-noise ratio for current or next-generation interferometer detectors could be high enough to detect such events in our Galaxy. Furthermore, we contrast the GW signals of AIC and rotating massive star iron core collapse and find that they can be distinguished, but only if the distance to the source is known and a detailed reconstruction of the GW time series from detector data is possible. Some of our AIC models form massive quasi-Keplerian accretion disks after bounce. The disk mass is very sensitive to progenitor mass and angular momentum distribution. In rapidly differentially rotating models whose precollapse masses are significantly larger than the Chandrasekhar mass, the resulting disk mass can be as large as $\sim 0.8 M_\odot$. Slowly and/or uniformly rotating models that are limited to masses near the Chandrasekhar mass produce much smaller disks or no disk at all. Finally, we find that the postbounce cores of rapidly spinning white dwarfs can reach sufficiently rapid rotation to develop a gravitorotational bar-mode instability. Moreover, many of our models exhibit sufficiently rapid and differential rotation to become subject to recently discovered low-$E_{\rm rot}/|W|$-type dynamical instabilities.

DOI: 10.1103/PhysRevD.81.044012 PACS numbers: 04.25.D−, 02.70.Bf, 04.30.Db, 97.60.Bw

I. INTRODUCTION

Single stars with main-sequence masses $M \lesssim 100 M_\odot$ end their nuclear-burning lives as electron-degenerate objects or with central electron-degenerate cores. More specifically, the end state is a carbon-oxygen or oxygen-neon white dwarf (WD) in the case of low-mass stars (i.e., with $M \lesssim 6$–$8 M_\odot$), or a degenerate oxygen-neon or iron core embedded in an extended nondegenerate stellar envelope in the case of more massive stars (i.e., 6–$8 M_\odot \lesssim M \lesssim 100 M_\odot$) (see, e.g., [1–3] and references therein). Electron-degenerate spherically symmetric objects become unstable to radial contraction once their mass exceeds the Chandrasekhar mass which, assuming zero temperature and no rotation, is given by $M_{\rm Ch} = 1.4575 (Y_e/0.5)^2 M_\odot$, where Y_e is the number of electrons per baryon, or ''electron fraction'' [4,5]. The effective Chandrasekhar mass $M_{\rm Ch,eff}$ of a WD or a stellar core increases somewhat with WD/core entropy (e.g., [2]) and can grow considerably by rotation, in which case it is limited only by the onset of nonaxisymmetric instability (e.g., [5–7]).

The iron core of a massive star is pushed over its Chandrasekhar limit by the ashes of silicon shell burning and undergoes collapse to a protoneutron star (PNS), accelerated by photodisintegration of heavy nuclei and elec-

tron capture [8]. In a high-density sub-$M_{\rm ch}$ oxygen-neon core of a less massive star, electron capture may decrease $M_{\rm Ch,eff}$, also leading to collapse [9,10]. In both cases, if an explosion results, the observational display is associated with a type II/Ibc supernova (SN).

On the other hand, a carbon-oxygen WD can be pushed over its stability limit through merger with or accretion from another WD (double-degenerate scenario) or by accretion from a nondegenerate companion star (single-degenerate scenario). Here, the WD generally experiences carbon ignition and thermonuclear runaway, leading to a type Ia SN and leaving no compact remnant [11]. However, at least theoretically, it is possible that massive oxygen-neon WDs[1] formed by accretion or merger, and, depending on initial mass, temperature, and accretion rate, also carbon-oxygen WDs, may grow to reach their $M_{\rm Ch,eff}$ or reach central densities sufficiently high ($\gtrsim 10^{9.7}$–10^{10} g cm^{-3}) for rapid electron capture to take place, triggering collapse to a PNS rather than thermonuclear explosion [7,10,15–25]. This may result in a peculiar, in most cases probably subenergetic, low-nickel-yield and short-lived transient [17,26–30]. This alternative to the type Ia SN scenario is called ''accretion-induced collapse'' (AIC) and will be the focus of this paper.

The details of the progenitor WD structure and formation and the fraction of all WDs that evolve to AICs are presently uncertain. Binary population synthesis models [25,31,32] and constraints on *r*-process nucleosynthetic yields from previous AIC simulations [27,33] predict AIC to occur in the Milky Way at a frequency of $\sim 10^{-5}$ to $\sim 10^{-8}$ yr^{-1} which is ~20–50 times less frequent than the expected rate of standard type Ia SNe (e.g., [34–37]). In part as a consequence of their rarity, but probably also due to their short duration and potentially weak electromagnetic display, AIC events have not been directly observed (but see [38,39], which discovered peculiar SNe that can be interpreted as resulting from AIC).

The chances of seeing a rare galactic AIC are dramatically boosted by the possibility of guiding electromagnetic observations by the detection of neutrinos and gravitational waves (GWs) emitted during the AIC process and a subsequent SN explosion. GWs, similar to neutrinos, are extremely difficult to observe, but can carry ''live'' dynamical information from deep inside electromagnetically opaque regions. The inherent multidimensional nature of GWs (they are lowest-order quadrupole waves) makes them ideal messengers for probing multidimensional dynamics such as rotation, turbulence, or neutron star pulsations [40–42]. The detection prospects for a GW burst from an AIC are significantly enhanced if theoretical knowledge of the expected GW signature of such an event is provided by computational modeling. In reverse, once a detection is made, detailed model predictions will make it possible to extract physical information on the AIC dynamics and the properties of the progenitor WD and, hence, will allow ''parameter estimation'' of the source.

Early spherically symmetric (one-dimensional, or 1D) simulations of AIC [26,43,44] and more recent axisymmetric (2D) ones [27–29] have demonstrated that the dynamics of AIC is quite similar to standard massive star core collapse: During collapse, the WD separates into a subsonically and homologously collapsing ($v \propto r$) inner core and a supersonically collapsing outer core. Collapse is halted by the stiffening of the equation of state (EOS) at densities near nuclear matter density and the inner-core rebounds into the still infalling outer core. An unshocked low-entropy PNS of inner-core material is formed. At its edge, a bounce shock is launched and initially propagates rapidly outward in mass and radius, but loses energy to the dissociation of heavy nuclei as well as to neutrinos that stream out from the optically thin postshock region. The shock stalls and, in the AIC case (but also in the case of the oxygen-neon core collapse in super-asymptotic-giant-branch stars [45,46]), is successfully revived by the deposition of energy by neutrinos in the postshock region (i.e., the ''delayed-neutrino mechanism'' [8,47]) or by a combination of neutrino energy deposition and magnetorotational effects in very rapidly rotating WDs [29]. But even without shock revival, explosion would occur when the WD surface layer is eventually accreted through the shock. Following the onset of explosion, a strong long-lasting neutrino-driven wind blows off the PNS surface, adding to the total explosion energy and establishing favorable conditions for *r*-process nucleosynthesis [26–29,48]. If the progenitor WD was rotating rapidly (and had a rotationally enhanced $M_{\rm Ch,eff}$), a quasi-Keplerian accretion disk of outer-core material may be left after the explosion [28]. Metzger *et al.* [30,49] recently proposed that this may lead to nickel-rich outflows that could significantly enhance the AIC observational display.

Rotating iron core collapse and bounce is the most extensively studied and best understood GW emission process in the massive star collapse context (see, e.g., [50] and the historical overview in [42]). However, most massive stars (perhaps up to ~99% in the local universe) are likely to be rather slow rotators that develop little asphericity during collapse and in the early postbounce phase [51–53] and produce PNSs that cool and contract to neutron stars with periods above ~10 ms and parameter $\beta = E_{\rm rot}/|W| \lesssim 0.1\%$ [53], where $E_{\rm rot}$ is the rotational kinetic energy and $|W|$ is the gravitational binding energy. This not only reduces the overall relevance of this emission process, but also diminishes the chances for postbounce gravitorotational nonaxisymmetric deformation of the PNS

[1]Previously, such WDs were expected to have a significant central ^{24}Mg mass fraction, and hence were referred to as oxygen-neon-magnesium WDs. Recent work based on up-do-date input physics and modern stellar evolution codes suggests that the mass fraction of ^{24}Mg is much smaller than previously thought (e.g., [12–14]).

which could boost the overall GW emission [42]. Axisymmetric rapidly rotating stars become unstable to nonaxisymmetric deformations if a nonaxisymmetric configuration with a lower total energy exists at a given β (see [54] for a review). The classical high-β instability develops in Newtonian stars on a dynamical time scale at $\beta \gtrsim \beta_{\rm dyn} \simeq 27\%$ (the general-relativistic value is $\beta \gtrsim 25\%$ [55,56]). A "secular" instability, driven by fluid viscosity or GW backreaction, can develop already at $\beta \gtrsim \beta_{\rm sec} \simeq 14\%$ [54]. Slower but strongly differentially rotating stars may also be subject to a nonaxisymmetric dynamical instability at β as small as $\sim 1\%$. This instability at low β was observed in a number of recent 3D simulations (e.g., [57–65]), and may be related to corotation instabilities in disks, but its nature and the precise conditions for its onset are presently not understood [66,67].

Stellar evolution theory and pulsar birth spin estimates suggest that most massive stars are rotating rather slowly (e.g., [51,53], but also [52,68] for exceptions). Hence, rotating collapse and bounce and nonaxisymmetric rotational instabilities are unlikely to be the dominant GW emission mechanisms in most massive star collapse events [42]. The situation may be radically different in AIC: Independent of the details of their formation scenario, AIC progenitors are expected to accrete significant amounts of mass and angular momentum in their pre-AIC evolutions [7,21–23,69]. They may reach values of β of up to $\sim 10\%$ prior to collapse, according to the recent work of Yoon and Langer [7,23], who studied the precollapse stellar structure and rotational configuration of WDs with sequences of 2D rotational equilibria. Depending on the distribution of angular momentum in the WD, rotational effects may significantly affect the collapse and bounce dynamics and lead to a large time-varying quadrupole moment of the inner core, resulting in a strong burst of GWs emitted at core bounce. In addition, the postbounce PNS may be subject to the high-β rotational instability (see [70,71] for an investigation via equilibrium sequences of PNSs formed in AIC) or to the recently discovered low-β instability.

Most previous (radiation-)hydrodynamic studies of AIC have either been limited to 1D [26,43,44] or were 2D, but did not use consistent 2D progenitor models in rotational equilibrium [27]. Fryer, Holz, and Hughes [72] presented the first estimates for the GW signal emitted by AIC based on one model of [27]. Drawing from the Yoon and Langer AIC progenitors [7,23], Dessart *et al.* [28,29] have recently performed 2D Newtonian AIC simulations with the multigroup flux-limited diffusion (MGFLD) neutrino-radiation-(M)HD code VULCAN/2D [73–75]. They chose two representative WD configurations for slow and rapid rotation with central densities of 5×10^{10} g cm^{-3} and total masses of $1.46 M_\odot$ and $1.92 M_\odot$. Both models were set up with the differential rotation law of [7,23]. The $1.46 M_\odot$ model had zero rotation in the inner core and rapid outer-core rotation while the $1.92 M_\odot$ was rapidly rotating throughout (ratio $\Omega_{\rm max,initial}/\Omega_{\rm center,initial} \sim 1.5$). Dessart *et al.* [28,29] found that rapid electron capture in the central regions of both models led to collapse to a PNS within only a few tens of milliseconds and reported successful neutrino-driven [28] and magnetorotational explosions [29] with final values of β (i.e., a few hundred milliseconds after core bounce) of $\sim 6\%$ and $\sim 26\%$, for the $1.46 M_\odot$ and $1.92 M_\odot$ models, respectively.[2] The analysis in [28,42,61] of the GW signal of the Dessart *et al.* models showed that the morphology of the AIC rotating collapse and bounce gravitational waveform is reminiscent of the so-called type III signal first discussed by Zwerger and Müller [76] and associated with small inner-core masses and a large pressure reduction at the onset of collapse in the latter's polytropic models.

In this paper, we follow a different approach from that of Dessart *et al.* [28,29]. We omit their detailed and computationally expensive treatment of neutrino radiation transport in favor of a simple, yet effective, deleptonization scheme for the collapse phase [77]. This simplification, while limiting the accuracy of our models at postbounce times $\gtrsim$ 5–10 ms, (i) enables us to study a very large set of precollapse WD configurations and their resulting AIC dynamics and GW signals and, importantly, (ii) allows us to perform these AIC simulations in general relativity, which is a crucial ingredient for the accurate modeling of dynamics in regions of strong gravity inside and near the PNS. Furthermore, as demonstrated by [50,78,79], general relativity is required for qualitatively and quantitatively correct predictions of the GW signal of rotating core collapse.

We focus on the collapse and immediate postbounce phase of AIC and perform an extensive set of 114 2D general-relativistic hydrodynamics simulations. We analyze systematically the AIC dynamics and the properties of the resulting GW signal. We explore the dependence of nonrotating and rotating AIC on the precollapse WD rotational setup, central density, core temperature, and core deleptonization, and study the resulting PNS's susceptibility to rotational nonaxisymmetric deformation. Furthermore, motivated by the recent work of Metzger *et al.* [30,49], who discussed the possible enhancement of the AIC observational signature by outflows from PNS accretion disks, we study the dependence of disk mass and morphology on WD progenitor characteristics and rotational setup.

We employ the general-relativistic hydrodynamics code COCONUT [78,80] and neglect MHD effects since they were shown to be small in the considered phases unless the precollapse magnetic field strength is extremely large ($B \gtrsim 10^{12}$ G, e.g., [29,81,82]). We employ a finite-temperature microphysical nuclear EOS in combination with the afore-

[2]These numbers are for the non-MHD simulations of [28]. In the MHD models of [29], an Ω dynamo builds up toroidal magnetic field, reducing the overall rotational energy and β.

mentioned deleptonization treatment of [77]. The precollapse 2D rotational-equilibrium WDs are generated according to the prescription of Yoon and Langer [7,23].

The plan of the paper is as follows. In Sec. II, we introduce the numerical methods employed and discuss the generation of our 2D rotational-equilibrium precollapse WD models as well as the parameter space of WD structure and rotational configuration investigated. In Sec. III, we discuss the overall AIC dynamics and the properties of the quasi-Keplerian accretion disks seen in many models. Section IV is devoted to a detailed analysis of the GW signal from rotating AIC. There, we also assess the detectability by current and future GW observatories and carry out a comparison of the GW signals of AIC and massive star iron core collapse. In Sec. V, we study the postbounce rotational configurations of the PNSs in our models and assess the possibility for nonaxisymmetric rotational instabilities. In Sec. VI, we present a critical summary and outlook.

II. METHODS AND INITIAL MODELS

A. The general-relativistic hydrodynamics code

We perform our simulations in 2 + 1 dimensions using the COCONUT code [80,83] which adopts the conformally flat approximation of general relativity [84]. This has been shown to be a very good approximation in the context of stellar collapse to PNSs [63,64,85]. COCONUT solves the metric equations as formulated in [86] using spectral methods as described in [80]. The relativistic hydrodynamics equations are solved via a finite-volume approach, piecewise parabolic reconstruction, and the Harten, Lax, van Leer, and Einfeld approximate Riemann solver [87]. COCONUT uses Eulerian spherical coordinates $\{r, \theta\}$ and for our purposes assumes axisymmetry. For the computational grid, we choose 250 logarithmically spaced, centrally condensed radial zones with a central resolution of 250 m and 45 equidistant angular zones covering 90°. We have performed test calculations with different grid resolutions to ascertain that the grid setup specified above is appropriate for our simulations. The space between the surface of the star and outer boundary of the finite difference grid is filled with an artificial atmosphere. We assume a constant density and stationary atmosphere in all zones where density drops below a prescribed threshold of 7×10^5 g cm^{-3}, a value marginally larger than the lowest-density value in the EOS table employed in our calculations (cf. Sec. II A 1). The atmosphere is reset after each time step in order to ensure that it adapts to the time-dependent shape of the stellar surface. We note that with the current computational setup COCONUT preserves integral quantities to sufficient precision with variations in the total angular momentum and rest mass below a few percent throughout an entire calculation. For further details of the formulations of the hydrodynamics and metric equations as well as their numerical implementation in COCONUT, the reader is referred to [50,80,86].

The version of COCONUT employed in this study does not include a nuclear reaction network. Hence, we, like Dessart *et al.* [28,29], ignore nuclear burning which may be relevant in the outer core of AIC progenitors where material is not in nuclear statistical equilibrium (NSE), but still sufficiently hot for oxygen/neon/magnesium burning to occur. This approximation is justified by results from previous work of [26,45] that included nuclear burning and did not observe a strong dynamical effect.

1. Equation of state

We make use of the finite-temperature nuclear EOS of Shen *et al.* (''Shen *et al.* EOS'' in the following, [88,89]) which is based on a relativistic mean-field model and is extended with the Thomas-Fermi approximation to describe the homogeneous phase of matter as well as the inhomogeneous matter composition. The parameter for the incompressibility of nuclear matter is 281 MeV and the symmetry energy has a value of 36.9 MeV. The Shen *et al.* EOS is used in tabulated fashion and in our version (equivalent to that used in [50,90]) includes contributions from baryons, electrons, positrons, and photons.

The Shen *et al.* EOS table used in our simulation has 180, 120, and 50 equidistant points in $\log_{10}\rho$, $\log_{10}T$, and Y_e, respectively. The table ranges are 6.4×10^5 g cm$^{-3} \leq \rho \leq 1.1 \times 10^{15}$ g cm^{-3}, 0.1 MeV $\leq T \leq 100.0$ MeV, and $0.015 \leq Y_e \leq 0.56$. Our variant of the Shen *et al.* EOS assumes that NSE holds throughout the entire $\{\rho, T, Y_e\}$ domain. In reality, NSE generally holds only at $T \gtrsim 0.5$ MeV. At lower temperatures, a nuclear reaction network and the advection of multiple chemical species and accounting for their individual ideal-gas contributions to the EOS is necessary for a correct thermodynamic description of the baryonic component of the fluid. However, since the electron component of the EOS is vastly dominant in the central regions of AIC progenitors (and also in the central regions of iron cores), the incorrect assumption of NSE at low temperatures can lead to only a small error in the overall (thermo)dynamics of the collapse and early postbounce phase.

2. Deleptonization during collapse and neutrino pressure

To account for the dynamically highly important change of the electron fraction Y_e by electron capture during collapse, we employ the approximate prescription proposed by Liebendörfer [77]. Liebendörfer's scheme is based on the observation that the local Y_e of each fluid element during the contraction phase can be rather accurately parametrized from full radiation-hydrodynamics simulations as a function of density alone. Liebendörfer demonstrated the effectiveness of this parametrization in the case of spherical symmetry, but also argued that it should still be reliable to employ a parametrization $\bar{Y}_e(\rho)$

obtained from a 1D radiation-hydrodynamics calculation in a 2D or 3D simulation, since electron capture depends more on local matter properties and less on the global dynamics of the collapsing core. On the basis of this argument, a $\bar{Y}_e(\rho)$ parametrization was applied in the rotating inner-core-collapse calculations of [50,63–65,79]. Here, we use the same implementation as discussed in [50] and track the changes in Y_e up to the point of core bounce. After bounce, we simply advect Y_e. Furthermore, as in [50], we approximate the pressure contribution due to neutrinos in the optically thick regime ($\rho \gtrsim 2 \times 10^{12}$ g cm^{-3}) by an ideal Fermi gas, following the prescription of [77]. This pressure contribution and the energy of the trapped neutrino radiation field are included in the matter stress-energy tensor and coupled with the hydrodynamics equations via the energy and momentum source terms specified in [64].

The deleptonization scheme described here is applicable only until core bounce and can track neither the postbounce neutrino burst (see, e.g., [91]) nor neutrino cooling/heating and the postbounce deleptonization of the PNS. The dynamics in the very early postbounce evolution (up to $\sim$10 ms) are unlikely to be dramatically affected by this limitation, but it should be kept in mind when interpreting results from later postbounce times.

For our AIC simulations we obtain $\bar{Y}_e(\rho)$ data from the 2D Newtonian radiation-hydrodynamics simulations carried out by Dessart *et al.* [28] with the VULCAN/2D code [73,74,82] in its MGFLD variant. We use these data because of their ready availability, but point out that the microphysics [92] used in VULCAN/2D does not yet include the updated electron capture rates of [93]. Moreover, VULCAN/2D presently does not treat velocity-dependent terms in the transport equation and neglects neutrino-electron scattering, both of which my have some impact on the evolution of Y_e in the collapse phase [91,94]. In Fig. 1 we plot representative $\bar{Y}_e(\rho)$ trajectories obtained from VULCAN/2D AIC simulations. At nuclear density, these data predict $Y_e \sim 0.18$, which is low compared to $Y_e \gtrsim 0.22$–0.26 seen in simulations of iron core collapse [50,77,91,94] and oxygen-neon core collapse [45]. This difference is not fully understood, but (i) could be physical and due to the WD initial data used here and in [28] or (ii) may be related to the radiation transport approximations and microphysics treatment in VULCAN/2D. To measure the importance of these uncertainties in $\bar{Y}_e(\rho)$, we perform calculations with systematic variations of $\bar{Y}_e(\rho)$ due either to changes in the precollapse WD temperature or to an *ad hoc* scaling (see Sec. II C 3).

Since AIC progenitors may be extremely rapidly rotating, it is not clear that the $\bar{Y}_e(\rho)$ parametrization is indeed independent of the specific model and rotational setup. The $\bar{Y}_e(\rho)$ trajectories shown in Fig. 1 result from the collapse simulations of the slowly rotating $1.46M_\odot$ model and of the rapidly rotating $1.92M_\odot$ model of Dessart *et al.* The very close agreement of the two curves suggests that rotational effects have only a small influence on the prebounce deleptonization and confirm the supposition of [77] at the level of the MGFLD and microphysics treatment in VULCAN/2D. All $\bar{Y}_e(\rho)$ data used in this study are available from [95].

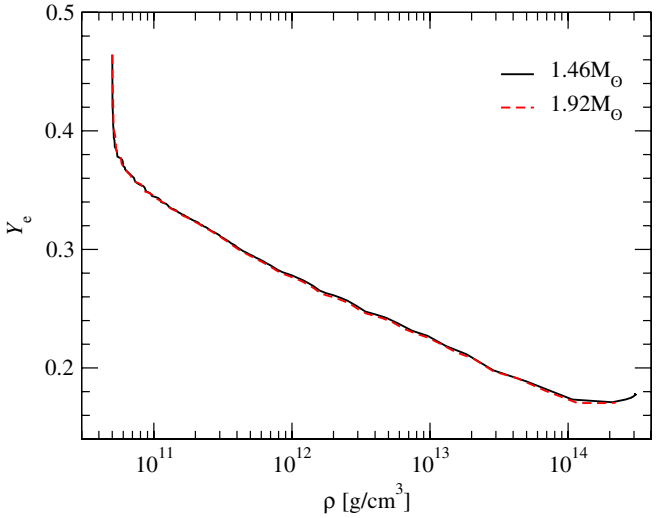

FIG. 1 (color online). Average electron fraction Y_e in the innermost 2 km in the collapsing WD as a function of density obtained from 2D MGFLD simulations with the VULCAN/2D code for models $1.46M_\odot$ and $1.92M_\odot$ of Dessart *et al.* [28]. Both models were set up with the same initial dependence of temperature on density and a temperature $T_0 = 1.0 \times 10^{10}$ K (see Sec. II B for details).

B. Precollapse white dwarf models

For constructing 2D WD models in rotational equilibrium with a given rotation law, we follow [23] and employ the self-consistent field (SCF) method [6,96–98] in Newtonian gravity. For the purpose of the SCF method, we assume that the WD is cold and has a constant Y_e of 0.5. After finding the 2D equilibrium configuration, we impose a temperature and Y_e distribution motivated by previous work [26,28]. Ideally, the WD initial model should be evolved in a multidimensional stellar evolution code with a finite-temperature EOS and accounting for weak processes such as neutrino cooling and electron capture. Because of the unavailability of such self-consistent AIC progenitors, we resort to the treatment that we discuss in detail in the remainder of this section.

1. Implementation of the self-consistent field method

Our implementation of the Newtonian SCF method has been tested by reproducing the WD models presented in [23,97], and finding excellent agreement. The compactness parameter GM/Rc^2 of the highest-density WD models considered here reaches $\sim 5 \times 10^{-3}$; hence general-relativistic effects at the precollapse stage are small and

the error introduced by Newtonian WD models is therefore negligible. Hereafter we will assume that the Newtonian mass of the equilibrium model represents the baryon mass accounted for when solving the general-relativistic equations.

The equation governing the stellar equilibrium is given by

$$\int \rho^{-1} dP + \Phi - \int \Omega^2 \varpi d\varpi = C, \tag{1}$$

where Φ is the gravitational potential, Ω is the angular velocity, ϖ is the radial cylindrical coordinate, and C is a constant that will be determined from boundary conditions using the SCF iterations as discussed below.

White dwarfs are stabilized against gravity by electron degeneracy pressure. For constructing precollapse WDs, we assume complete degeneracy for which the WD EOS (e.g., [6]) is given by

$$\begin{aligned} P &= A[x(2x^2 - 3)(x^2 + 1)^{1/2} + 3\sinh^{-1} x]; \\ x &= (\rho/B)^{1/3}, \end{aligned} \tag{2}$$

where $A = 6.01 \times 10^{22}$ dyn cm^{-2} and $B = 9.82 \times 10^5 Y_e^{-1}$ g cm^{-3}. We set $Y_e = 0.5$, assuming at this stage that no electron capture has taken place. The integral $\int \rho^{-1} dP$ in Eq. (1) is the enthalpy H which, given our choice of WD EOS, can be expressed analytically as

$$H = \frac{8A}{B}\left[1 + \left(\frac{\rho}{B}\right)^{2/3}\right]. \tag{3}$$

With this, Eq. (1) trivially becomes

$$H = C - \Phi + \int \Omega^2 \varpi d\varpi. \tag{4}$$

Following the SCF method, we proceed to first produce a trial density distribution $\rho(r, \theta)$ and impose a rotation law (discussed in the following Sec. II B 2).

We then calculate C by using the value for the maximum density and the angular velocity at the center of the star $\Omega(\varpi = 0) = \Omega_{\rm c,i}$. Based on the trial density distribution, we calculate H via Eq. (4) and then update the density distribution based on H using the analytic expression (3). This updated density distribution in turn results in a new value for H. We iterate this procedure until all the maximum absolute values of three relative differences of H, Ω, and ρ become less than 10^{-3}.

2. Progenitor rotational configuration

Our axisymmetric progenitor WD models are assumed either to be in uniform rotation or to follow the differential rotation law proposed by Yoon and Langer [23]. The latter argued that the rotation law of a WD that accretes matter at high rates ($> 10^{-7} M_\odot$ yr^{-1}) is strongly affected by angular momentum transport via the dynamical shear instability (DSI) in the inner region, and due to the secular shear instability (as well as Eddington-Sweet circulations [99]) in the outer layers. According to their results, the shear rate in the core remains near the threshold value for the onset of the DSI. This results in a characteristic rotation law which has an absolute maximum in the angular velocity just above the shear-unstable core. We define $\varpi_{\rm p}$ as the position of this maximum. This position is linked to layers with a density as low as several percent of the WD central density so that

$$\rho_{\rm i}(\varpi = \varpi_{\rm p}, z = 0) = f_{\rm p} \rho_{\rm c,i}, \tag{5}$$

and where, following [23,28], we choose $f_{\rm p} = \{0.05, 0.1\}$ in our models. (Note that the differential rotation law adopted for the models of [28] had $f_{\rm p} = 0.05$.) In the inner regions with $\varpi < \varpi_{\rm p}$, we have

$$\Omega(\varpi) = \Omega_{\rm c,i} + \int_0^{\varpi} \frac{f_{\rm sh} \sigma_{\rm DSI,crit}}{\varpi'} d\varpi', \tag{6}$$

where $\Omega_{\rm c,i}$ is the angular velocity at the center and $\sigma_{\rm DSI,crit}$ is the threshold value of the shear rate in the inner core for the onset of the DSI. $f_{\rm sh}$ is a dimensionless parameter (≤ 1.0) describing the deviation of the shear rate from $\sigma_{\rm DSI,crit}$. We compute $\sigma_{\rm DSI,crit}$ assuming homogeneous chemical composition and constant temperature, in which case $\sigma_{\rm DSI,crit}$ can be estimated as [cf. Eq. (7) of [7]]

$$\sigma^2_{\rm DSI,crit} \simeq 0.2 \left(\frac{g}{10^9 \text{ cm s}^{-2}}\right)\left(\frac{\delta}{0.01}\right)\left(\frac{H_{\rm p}}{8 \times 10^7 \text{ cm}}\right)^{-1}\left(\frac{\nabla_{\rm ad}}{0.4}\right), \tag{7}$$

where g is the free-fall acceleration, $H_{\rm p}$ is the pressure scale height ($= -dr/d\ln P$), $\nabla_{\rm ad}$ is the adiabatic temperature gradient [$= -(\partial \ln T/\partial \ln P)_s$ where s is the specific entropy], and $\delta = (\partial \ln \rho/\partial \ln T)_P$. The quantities δ, $H_{\rm p}$, and $\nabla_{\rm ad}$ are computed using the routines of Blinnikov, Dunina-Barkovskaya, and Nadyozhin [100].

At the equatorial surface, the WD is assumed to rotate at a certain fraction $f_{\rm K}$ of the local Keplerian angular velocity $\Omega_{\rm K}$:

$$\Omega(R_{\rm e}) = f_{\rm K} \Omega_{\rm K}(R_{\rm e}), \tag{8}$$

where $R_{\rm e}$ is the equatorial radius of the WD and where we have set $f_{\rm K} = 0.95$. In the region between $\varpi_{\rm p}$ and $R_{\rm e}$, we again follow [23] and adopt the following rotation law:

$$\Omega(\varpi)/\Omega_{\rm K} = \Omega(\varpi_{\rm p})/\Omega_{\rm K}(\varpi_{\rm p}) + \mathcal{C}(\varpi - \varpi_{\rm p})^a, \tag{9}$$

where the constant $\mathcal{C}$ is determined for a given value of a as

$$\mathcal{C} = \frac{f_{\rm K} - \Omega(\varpi_{\rm p})/\Omega_{\rm K}(\varpi_{\rm p})}{(R_{\rm e} - \varpi_{\rm p})^a}. \tag{10}$$

The choice of the exponent a does not have a strong impact on the WD structure because of the constraints imposed by $\Omega(\varpi_{\rm p})$ and $\Omega(R_{\rm e})$ at each boundary. In our study, we adopt $a = 1.2$. For further details, we refer the reader to Sec. 2.2 of [23].

Saio and Nomoto [22] argued that turbulent viscosity resulting from a combination of a baroclinic instability (see, e.g., [101]; neglected by Yoon and Langer [7,23]) and the DSI is so efficient in transporting angular momentum that the angular velocity becomes nearly uniform in the WD interior, while only surface layers with mass $\lesssim 0.01 M_\odot$ rotate differentially [22]. Piro [102], who also considered angular momentum transport by magnetic stresses, confirmed these results. Hence, in order to study the suggested case of uniform precollapse WD rotation, we complement our differentially rotating WD models with a set of uniformly rotating AIC progenitors.

3. Initial temperature profile

Because our initial models are constructed by imposing hydrostatic equilibrium [Eq. (1)] with a barotropic EOS [Eq. (2)], the WD structure is independent of temperature. However, the latter is needed as input for the finite-temperature nuclear EOS used in our AIC simulations. We follow Dessart *et al.* [28] and impose a scaling of the temperature with density according to

$$T(\varpi, z) = T_0[\rho_{\rm c,i}/\rho(\varpi, z)]^{0.35}, \tag{11}$$

where (ϖ, z) are cylindrical coordinates and ρ_0 is the density at which the stellar temperature equals T_0.

4. Initial electron fraction profile

For the purpose of constructing AIC progenitor WDs in rotational equilibrium, we assume that no electron capture has yet taken place and set $Y_e = 0.5$. A real AIC progenitor, however, will have seen some electron captures on Ne/Mg/Na nuclei (e.g., [10]) before the onset of dynamical collapse. In addition, electrons will be captured easily by free protons that are abundant at the temperatures of the WD models considered here. Hence, a Y_e of 0.5 is rather inconsistent with real WD evolution. Dessart *et al.* [28], who started their simulations with $Y_e = 0.5$ models, observed an early burst of electron capture. This led to a significant initial drop of Y_e that leveled off after 5–10 ms beyond which the Y_e profile evolved in qualitatively similar fashion to what is known from iron core collapse (see Fig. 1, which depicts this drop of Y_e at low densities). To account for this, we adopt as initial $\bar{Y}_e(\rho)$ a parametrization obtained from the equatorial plane of the models of Dessart *et al.* [28] at ~7 ms into their evolution when the initial electron capture burst has subsided. We use these $\bar{Y}_e(\rho)$ data for the Y_e evolution of the low-density ($\rho < \rho_{\rm c,i}$) part of the WD during collapse.

C. Parameter space

The structure and thermodynamics of the AIC progenitor and the resulting dynamics of the collapse depend on a variety of parameters that are constrained only weakly by theory and observation (e.g., [7,19,23]). Here, we study the dependence on the central density, rotational configuration, and core temperature. In the following we lay out our parameter choices and discuss the nomenclature of our initial models whose key properties we summarize in Table I.

1. Progenitor white dwarf central density

In order to investigate the impact of the precollapse central WD density $\rho_{\rm c,i}$ on the collapse dynamics, we consider sequences of WD models with central densities in the range from 4×10^9 g cm^{-3} to 5×10^{10} g cm^{-3}. This range of densities is motivated by previous studies arguing that WDs in this range of $\rho_{\rm c,i}$ may experience AIC [7,19,28].

We therefore choose a set of four central densities, i.e., 4×10^9, 1×10^{10}, 2×10^{10}, 5×10^{10} g cm^{-3}, and correspondingly begin our model names with letters A, B, C, D. We perform AIC simulations of nonrotating (spherically symmetric) WDs with central density choices A–D and restrict the rotating models to the limiting central density choices A and D.

In Fig. 2 we plot radial density profiles of our nonrotating WD models to show the strong dependence of the WD compactness on the choice of central density. This aspect will prove important for the understanding of the collapse dynamics of rapidly rotating models.

2. Progenitor white dwarf rotational configuration

Since the rotational configuration of AIC progenitor WDs is constrained only poorly, we consider uniformly rotating ($\Omega_{\rm i} = \Omega_{\rm c,i}$ everywhere) as well as a variety of differentially rotating WD configurations. To denote the general rotation type, we use the letter U (D) for uniform (differential) rotation as the second letter in each model name.

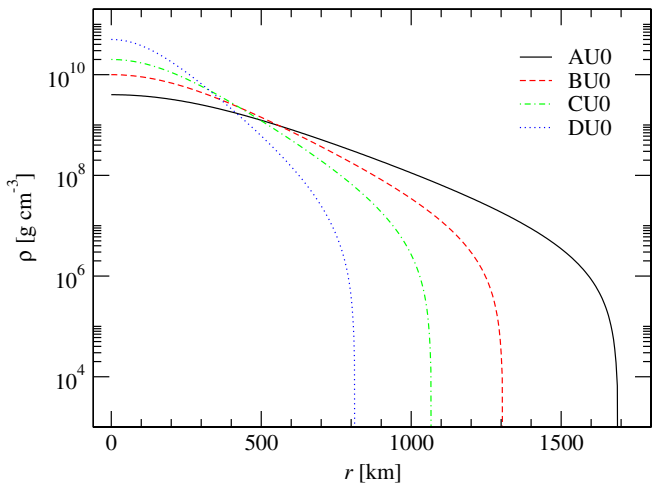

FIG. 2 (color online). The radial profile of the rest-mass density for nonrotating white dwarf models AU0, BU0, CU0, and DU0.

TABLE I. Summary of the initial WD models: $\Omega_{c,i}$ is the central angular velocity and $\Omega_{max,i} = \Omega(\varpi_p)$, M_0 is the total rest mass, and J is the total angular momentum. $|W_i|$ and $E_{rot,i}$ are the gravitational energy and rotational kinetic energy of the WD, respectively. R_e and R_p are the equatorial and polar radii.

Initial model	$\Omega_{c,i}$ [rad/s]	$\Omega_{max,i}$ [rad/s]	$\rho_{c,i}$ [10^{10} g cm^{-3}]	M_0 [$M_\odot$]	J [10^{50} ergs]	$\lvert W_i\rvert$ [10^{50} ergs]	$E_{rot,i}$ [10^{50} ergs]	β_i [%]	R_e [km]	R_e/R_p
AU0	0.000	0.000	0.4	1.390	0.00	37.32	0.00	0.00	1692	1.000
AU1	1.000	1.000	0.4	1.394	0.09	37.50	0.04	0.11	1710	0.988
AU2	1.800	1.800	0.4	1.405	0.16	37.90	0.15	0.38	1757	0.953
AU3	2.000	2.000	0.4	1.409	0.18	38.04	0.18	0.48	1775	0.943
AU4	3.000	3.000	0.4	1.437	0.29	39.04	0.44	1.12	1938	0.848
AU5	3.500	3.500	0.4	1.458	0.36	39.78	0.64	1.60	2172	0.748
BU0	0.000	0.000	1.0	1.407	0.00	51.44	0.00	0.00	1307	1.000
CU0	0.000	0.000	2.0	1.415	0.00	65.28	0.00	0.00	1069	1.000
DU0	0.000	0.000	5.0	1.421	0.00	89.11	0.00	0.00	813	1.000
DU1	2.000	2.000	5.0	1.423	0.03	89.25	0.03	0.04	817	0.995
DU2	3.000	3.000	5.0	1.425	0.05	89.42	0.08	0.09	822	0.988
DU3	3.500	3.500	5.0	1.426	0.06	89.53	0.11	0.12	825	0.983
DU4	5.000	5.000	5.0	1.432	0.09	90.00	0.22	0.24	840	0.963
DU5	7.000	7.000	5.0	1.442	0.13	90.87	0.44	0.49	871	0.920
DU6	9.000	9.000	5.0	1.458	0.17	92.12	0.77	0.83	931	0.853
DU7	9.500	9.500	5.0	1.462	0.18	92.50	0.86	0.94	956	0.828
AD1	0.000	2.881	0.4	1.434	0.28	38.74	0.41	1.07	2344	0.71
AD2	0.327	3.204	0.4	1.443	0.31	39.04	0.49	1.26	2382	0.69
AD3	1.307	4.198	0.4	1.477	0.42	40.25	0.81	2.01	2521	0.64
AD4	2.287	5.174	0.4	1.526	0.56	42.01	1.27	3.01	2707	0.58
AD5	3.000	5.903	0.4	1.575	0.69	43.77	1.74	3.97	2888	0.54
AD6	3.267	6.173	0.4	1.595	0.75	44.47	1.95	4.38	2964	0.53
AD7	3.920	6.833	0.4	1.659	0.93	46.77	2.59	5.55	3200	0.47
AD8	4.247	7161	0.4	1.706	1.05	48.45	3.02	6.24	3366	0.44
AD9	5.227	8.155	0.4	1.884	1.58	54.69	4.88	8.92	4008	0.35
AD10	5.554	8.485	0.4	1.974	1.87	57.80	5.85	10.13	4338	0.313
DD1	0.000	7.688	5.0	1.446	0.13	90.85	0.51	0.60	1097	0.73
DD2	3.000	10.70	5.0	1.467	0.19	92.52	0.95	1.00	1156	0.69
DD3	6.000	13.73	5.0	1.498	0.26	95.05	1.61	1.70	1238	0.63
DD4	9.000	16.74	5.0	1.544	0.35	98.70	2.57	2.60	1353	0.56
DD5	12.00	19.77	5.0	1.612	0.48	104.08	4.01	3.90	1528	0.48
DD6	15.00	22.81	5.0	1.716	0.68	111.95	6.31	5.60	1819	0.39
DD7	18.00	25.84	5.0	1.922	1.10	126.69	10.77	8.50	2430	0.28
AD1f1	0.000	2.305	0.4	1.422	0.23	38.33	0.30	0.79	2283	0.730
AD1f2	0.000	1.723	0.4	1.413	0.19	38.03	0.22	0.58	2233	0.753
AD1f3	0.000	1.152	0.4	1.406	0.15	37.79	0.16	0.41	2188	0.770
AD1f4	0.000	0.576	0.4	1.401	0.11	37.64	0.11	0.29	2151	0.785
AD3f1	1.307	3.610	0.4	1.457	0.36	39.56	0.62	1.58	2434	0.673
AD3f2	1.307	3.032	0.4	1.441	0.31	39.01	0.47	1.22	2361	0.700
AD3f3	1.307	2.457	0.4	1.428	0.26	38.56	0.36	0.90	2298	0.723
AD3f4	1.307	1.883	0.4	1.417	0.21	38.20	0.26	0.70	2243	0.745
AD6f1	3.267	5.574	0.4	1.555	0.64	43.13	1.54	3.57	2798	0.555
AD6f2	3.267	5.003	0.4	1.522	0.55	41.96	1.23	2.93	2666	0.590
AD6f3	3.267	4.423	0.4	1.494	0.47	41.00	0.97	2.37	2554	0.625
AD6f4	3.267	3.842	0.4	1.472	0.41	40.20	0.76	1.89	2462	0.655
AD9f1	5.227	7.564	0.4	1.772	1.23	50.92	3.71	7.28	3574	0.400
AD9f2	5.227	6.978	0.4	1.691	1.00	48.13	2.89	6.01	3264	0.448
AD9f3	5.227	6.392	0.4	1.630	0.84	46.00	2.29	4.98	3029	0.493
AD9f4	5.227	5.808	0.4	1.584	0.71	44.38	1.83	4.12	2851	0.533
AD10f1	5.554	7.896	0.4	1.833	1.41	53.06	4.35	8.20	3793	0.370
AD10f2	5.554	7.305	0.4	1.741	1.13	49.93	3.37	6.74	3434	0.420
AD10f3	5.554	7.721	0.4	1.665	0.93	47.28	2.64	5.58	3149	0.468
AD10f4	5.554	6.134	0.4	1.611	0.78	44.40	2.10	4.62	2942	0.510
AD11f2	6.000	7.756	0.4	1.815	1.35	52.60	4.16	7.90	3696	0.380
AD12f3	7.000	8.175	0.4	1.914	1.65	56.27	4.23	9.30	4010	0.340
AD12f4	7.000	7.586	0.4	1.798	1.29	52.29	3.99	7.64	3574	0.393
AD13f4	8.000	8.585	0.4	2.049	2.09	61.30	6.75	11.01	4436	0.295

The low-density uniformly rotating model sequence AU{1–5} is set up with initial angular velocities $\Omega_{c,i}$ from 1 to 3.5 rad s^{-1}, where the latter value corresponds to rotation very close to the mass-shedding limit. The more compact uniformly rotating sequence DU{1–7} is set up with precollapse $\Omega_{c,i}$ from 2 to 9.5 rad s^{-1}, where, again, the latter value corresponds to near-mass-shedding rotation.

Model sequences AD{1–10}, DD{1–7} are differentially rotating according to the rotation law discussed in Sec. II B 2 and specified by Eqs. (6) and (9), with the parameter choice $f_{sh} = 1$ and $f_p = 0.1$ for the AD sequence and $f_{sh} = 1$ and $f_p = 0.05$ for the DD sequence. We recall that f_p is the fraction of the central density where the angular velocity has a global maximum. While $f_p = 0.1$ is the standard choice of [23], we adopt $f_p = 0.05$ for the high-density sequence DD to be in line with the parameter choices made for the models of Dessart *et al.* [28]. Test calculations with AD models show that the variation of f_p between 0.05 and 0.10 affects the rotational configuration of the outer WD layers only and does not have any appreciable effect on the AIC dynamics. For the AD{1–10} sequence, we chose $\Omega_{c,i}$ in the range from 0 to 5.6 rad s^{-1}, resulting in maximum angular velocities $\Omega_{max,i}$ in the range of 2.88 to 8.49 rad s^{-1}. The higher-density DD{1–7} sequence rotates with $\Omega_{c,i}$ in the range from 0 to 18 rad s^{-1}, corresponding to maximum Ω in the range of 7.69 to 25.84 rad s^{-1}. The values of $\Omega_{c,i}$ and $\Omega_{max,i}$ for the individual AD and DD models are given in Table I. As representative examples resulting from our assumed rotation law, we plot in Fig. 3 for models AD3, AD5, and AD10 the angular velocity and the ratio of the angular velocity to the local Keplerian value as a function of cylindrical radius and of the enclosed rest mass. In Fig. 4, we plot the color maps of the rest-mass density on the $r - \theta$ plane for the representative precollapse WD models AD1, AD5, and AD10.

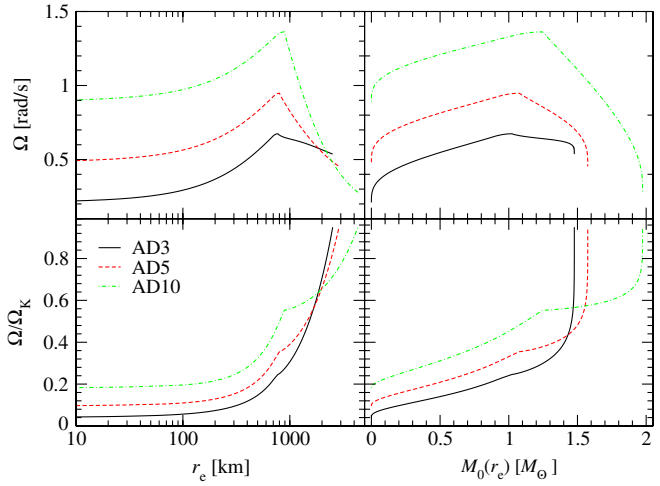

FIG. 3 (color online). Upper panels: angular velocity as a function of equatorial radius (left panel) and enclosed mass coordinate (right panel) for three representative precollapse WD models AD3, AD5, and AD10. Lower panels: angular velocity normalized to the local Keplerian value as a function of equatorial radius and enclosed mass for the same models.

In order to study the effect of variations in the degree of differential rotation, we vary the dimensionless shear parameter f_{sh} for a subsequence of AD models and append suffixes $f\{1–4\}$ to their names corresponding to $f_{sh} = \{0.8, 0.6, 0.4, 0.2\}$, respectively. Figure 5 shows the behavior of the initial angular velocity distribution with decreasing f_{sh} in the rapidly differentially rotating model AD10.

An important point to mention is the large range of precollapse WD masses covered by our models. Depending on the initial central density and the rotational setup, our WDs' masses range from a sub-M_{Ch} value of $1.39M_\odot$ in the nonrotating low-$\rho_{c,i}$ model AU0 to a rotationally supported super-M_{Ch} mass of $2.05M_\odot$ in the rapidly differentially rotating model AD13f4. The maximum mass in our sequence of uniformly rotating WDs is $1.462M_\odot$ and is obtained in model DU7.

To conclude the discussion of our initial rotational configurations, we present in Fig. 6 for all models the initial values (β_i) of the parameter β as a function of their precollapse central angular velocity $\Omega_{c,i}$. Differentially rotating WD models can reach β_i of up to $\sim$10% while staying below the mass-shedding limit. This number is more than a factor of 2 larger than what seems possible in massive star iron core collapse (see, e.g., [50]), making these rapidly rotating AIC progenitor models potential candidates for a dynamical nonaxisymmetric rotational instability during their postbounce AIC evolution (see Sec. V).

3. Progenitor white dwarf core temperature and $\bar{Y}_e(\rho)$ parametrization

We use Eq. (11) to set up the initial temperature distribution as a function of density. Dessart *et al.* chose $\rho_0 = \rho_{c,i}$ ($= 5 \times 10^{10}$ g cm^{-3} in their models) and $T_0 = 10^{10}$ K for their $1.46M_\odot$ model, and $T_0 = 1.3 \times 10^{10}$ K for their $1.92M_\odot$ model. These values (i) are similar to what was used in the earlier work of Woosley and Baron [26] and (ii) work well with the tabulated EOS employed and the assumption of NSE, but may be higher than the temperatures prevailing in accreting precollapse WDs in nature (see, e.g., [7,10,22]).

While the fluid pressure is affected very little by different temperature distributions, this is not the case for the free proton fraction which increases strongly with T in the range from 10^9 to 10^{10} K and at precollapse core densities. This increase of the proton fraction can lead to enhanced electron capture during AIC and in this way may have a significant influence on the AIC dynamics. In order to test the sensitivity of our AIC simulations on the assumed T_0,

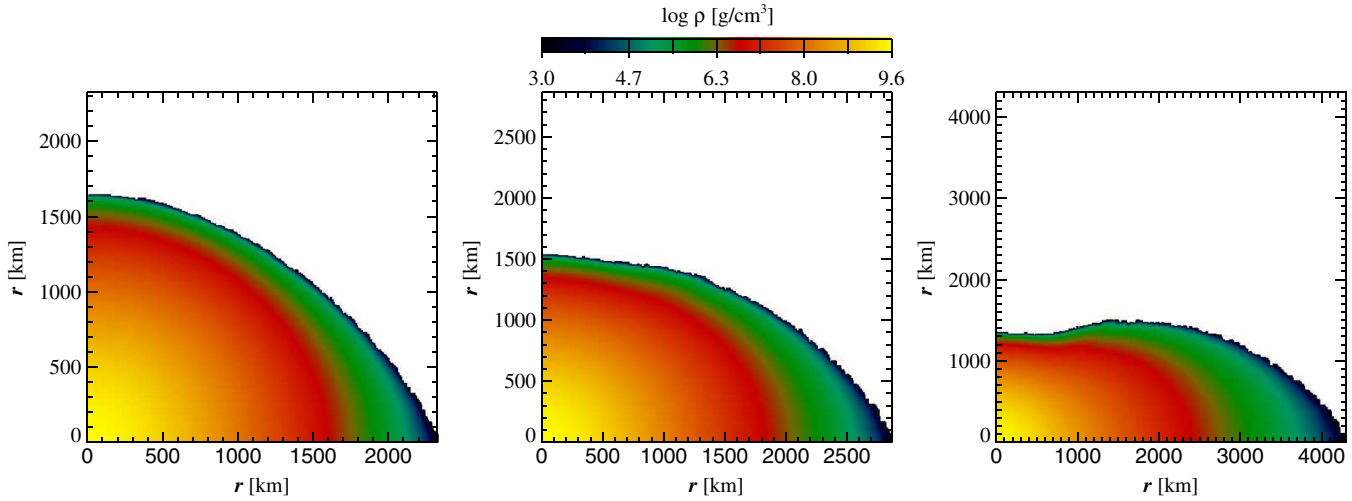

FIG. 4 (color online). Color map of the rest-mass density for the precollapse white dwarf models AD1 (left panel), AD5 (center panel), and AD10 (right panel). The apparent ruggedness of the WD surface layers is a result of the finite resolution of our computational grid and the mapping procedure in the visualization tool. The ruggedness has no influence on the collapse and postbounce dynamics of the inner core.

we not only study models with $T_0 = 10^{10}$ K (at $\rho_0 = 5 \times 10^{10}$ g cm^{-3}, hereafter the "high-T" models), but perform also simulations for models set up with $T_0 = 5 \times 10^9$ K (at $\rho_0 = 5 \times 10^{10}$ g cm^{-3}, hereafter the "low-T" models). To obtain the $\bar{Y}_e(\rho)$ parametrization (see Sec. II A 2) for the latter temperature, we reran with VULCAN/2D the $1.46 M_\odot$ AIC model of Dessart *et al.* up to core bounce with the same setup as discussed in [28], but using the lower value of T_0. We do not indicate the two different initial temperatures in the model names, but list the results obtained in the two cases side-by-side in Table II.

In addition to variations in deleptonization due to differences in the precollapse WD thermodynamics, we must also consider the possibility of unknown systematic biases that lead to small values of Y_e in the inner core at bounce (see Sec. II A 2). In order to study the effect that larger values of Y_e in the inner core have on the AIC dynamics, we perform a set of test calculations with scaled $\bar{Y}_e(\rho)$ trajectories. We implement this by making use of the fact that $Y_e(\rho)$ is to good approximation a linear function of $\log(\rho)$ (see Fig. 1). We change the slope of this function between $\rho = 5 \times 10^{10}$ g cm^{-3} and $\rho = 2.5 \times 10^{14}$ g cm^{-3} by increasing $Y_e(\rho = 2.5 \times 10^{14}$ g cm$^{-3})$ by 10% and 20%. We pick these particular scalings, since the 20% increase yields inner-core values of Y_e at bounce that are very close to those obtained in 1D Boltzmann neutrino transport simulations of oxygen-neon core collapse

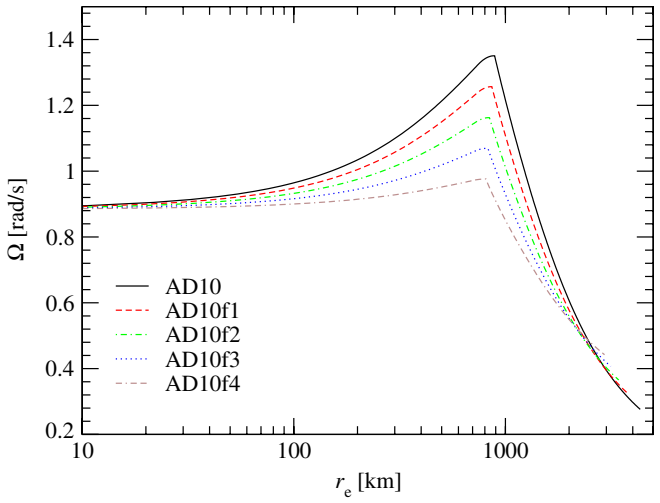

FIG. 5 (color online). Angular velocity as a function of equatorial radius for model AD10 and varying values of the dimensionless shear parameter $f_{\rm sh}$ that controls the rate at which the angular velocity increases with ϖ in the region $\varpi < \varpi_{\rm p}$.

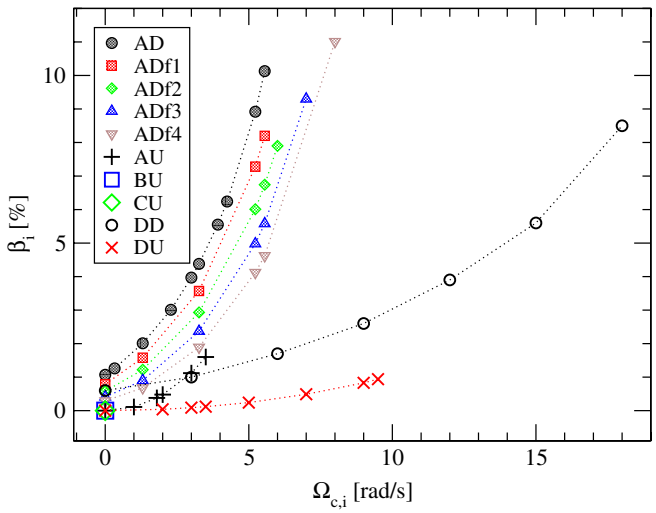

FIG. 6 (color online). Parameter $\beta_{\rm i}$ versus central angular velocity $\Omega_{\rm c,i}$ for our AIC progenitor WD model set.

TABLE II. Summary of key quantitative results from our AIC simulations. $\rho_{\rm max,b}$ is the maximum density in the core at the time of bounce $t_{\rm b}$, $|h|_{\rm max}$ is the peak value of the GW signal amplitude, while $\beta_{\rm ic,b}$ is the inner-core parameter β at bounce. Models marked by unfilled/filled circles ($\circ$ / $\bullet$) undergo a pressure-dominated bounce with/without significant early postbounce convection. Models marked with the cross sign ($\times$) undergo centrifugal bounce at subnuclear densities. The values left/right of the vertical separator (|) are for the models with low/high temperature profiles.

Collapse model		$\rho_{\rm max,b}$ [10^{14} g cm^{-3}]	$t_{\rm b}$ [ms]	$\lvert h\rvert_{\rm max}$ [10^{-21} at 10 kpc]	$\beta_{\rm ic,b}$ [%]
AU0	$\circ\vert\circ$	2.782|2.807	214.1|204.9	0.27|0.20	0.00|0.00
AU1	$\bullet\vert\bullet$	2.697|2.719	214.9|205.5	0.78|0.62	1.27|1.20
AU2	$\bullet\vert\bullet$	2.628|2.629	216.7|206.9	2.33|1.90	3.75|3.56
AU3	$\bullet\vert\bullet$	2.610|2.613	217.3|207.4	2.79|2.29	4.49|4.28
AU4	$\bullet\vert\bullet$	2.525|2.508	221.4|210.8	5.01|4.23	8.48|8.19
AU5	$\bullet\vert\bullet$	2.461|2.444	224.2|212.9	5.90|5.05	10.46|10.17
BU0	$\circ\vert\circ$	2.805|2.800	100.9|95.3	0.19|0.16	0.00|0.00
CU0	$\circ\vert\circ$	2.782|2.788	56.3|51.4	0.20|0.24	0.00|0.00
DU0	$\circ\vert\circ$	2.797|2.781	27.5|25.2	0.34|0.42	0.00|0.00
DU1	$\circ\vert\circ$	2.786|2.777	27.6|25.2	0.23|0.27	0.18|0.17
DU2	$\circ\vert\circ$	2.774|2.763	27.6|25.2	0.24|0.31	0.39|0.38
DU3	$\circ\vert\circ$	2.756|2.758	27.6|25.2	0.31|0.27	0.53|0.51
DU4	$\bullet\vert\bullet$	2.728|2.719	27.6|25.3	0.64|0.55	1.07|1.03
DU5	$\bullet\vert\bullet$	2.669|2.658	27.7|25.3	1.21|1.07	2.04|1.97
DU6	$\bullet\vert\bullet$	2.642|2.640	27.8|25.4	1.97|1.73	3.27|3.17
DU7	$\bullet\vert\bullet$	2.627|2.619	27.9|25.5	2.17|1.92	3.61|3.50
AD1	$\bullet\vert\bullet$	2.661|2.679	218.7|208.5	2.24|1.75	2.96|2.62
AD2	$\bullet\vert\bullet$	2.620|2.616	220.1|209.5	2.85|2.30	3.93|3.55
AD3	$\bullet\vert\bullet$	2.547|2.547	225.5|213.7	4.62|3.93	7.20|6.71
AD4	$\bullet\vert\bullet$	2.447|2.442	232.9|219.4	5.89|5.19	10.58|10.01
AD5	$\bullet\vert\bullet$	2.361|2.389	241.1|225.5	6.37|5.68	13.09|12.33
AD6	$\bullet\vert\bullet$	2.324|2.355	246.7|229.7	6.39|5.78	14.03|13.18
AD7	$\bullet\vert\bullet$	2.226|2.228	260.0|238.8	6.00|5.73	16.34|15.23
AD8	$\bullet\vert\bullet$	2.145|2.167	264.3|240.9	6.01|5.70	17.48|16.30
AD9	$\times\vert\times$	1.817|1.911	319.7|267.3	3.40|4.00	23.38|20.69
AD10	$\times\vert\times$	1.629|1.790	393.6|284.5	2.36|3.54	24.41|21.25
DD1	$\circ\vert\circ$	2.779|2.772	27.5|25.2	0.46|0.37	0.70|0.58
DD2	$\bullet\vert\bullet$	2.684|2.686	27.7|25.3	1.24|1.06	1.95|1.81
DD3	$\bullet\vert\bullet$	2.642|2.638	27.8|25.5	2.41|2.08	3.76|3.56
DD4	$\bullet\vert\bullet$	2.586|2.571	28.1|25.7	3.78|3.29	5.93|5.71
DD5	$\bullet\vert\bullet$	2.526|2.498	28.4|25.9	5.22|4.61	8.27|8.09
DD6	$\bullet\vert\bullet$	2.457|2.425	28.8|26.3	6.52|5.82	10.57|10.51
DD7	$\bullet\vert\bullet$	2.389|2.352	29.2|26.5	7.58|6.81	12.75|12.79
AD1f1	$\bullet\vert\bullet$	2.718|2.733	217.1|207.2	1.57|1.24	2.06|1.80
AD1f2	$\bullet\vert\bullet$	2.759|2.767	215.8|206.2	0.96|0.75	1.26|1.10
AD1f3	$\circ\vert\circ$	2.787|2.795	214.9|205.5	0.47|0.36	0.59|0.49
AD1f4	$\circ\vert\circ$	2.803|2.803	214.4|205.0	0.26|0.18	0.14|0.12
AD3f1	$\bullet\vert\bullet$	2.560|2.564	222.5|211.5	4.09|3.41	6.26|5.81
AD3f2	$\bullet\vert\bullet$	2.583|2.597	220.1|209.6	3.46|2.85	5.23|4.85
AD3f3	$\bullet\vert\bullet$	2.622|2.631	218.2|208.1	2.76|2.25	4.17|3.87
AD3f4	$\bullet\vert\bullet$	2.656|2.662	216.7|207.0	2.03|1.63	3.10|2.90
AD6f1	$\bullet\vert\bullet$	2.356|2.377	237.6|222.9	6.47|5.77	13.20|12.52
AD6f2	$\bullet\vert\bullet$	2.395|2.399	233.1|219.7	6.41|5.63	12.31|11.79
AD6f3	$\bullet\vert\bullet$	2.421|2.424	229.1|216.7	6.28|5.43	11.47|11.06
AD6f4	$\bullet\vert\bullet$	2.463|2.444	225.7|214.1	5.95|5.12	10.56|10.20
AD9f1	$\times\vert\times$	1.913|1.994	282.0|250.9	3.88|5.77	20.80|18.84
AD9f2	$\bullet\vert\bullet$	2.000|2.073	265.1|241.7	5.25|6.17	20.10|18.09
AD9f3	$\bullet\vert\bullet$	2.092|2.115	253.9|234.6	6.96|6.41	18.44|17.45
AD9f4	$\bullet\vert\bullet$	2.159|2.166	244.7|228.3	7.30|6.74	17.67|16.74
AD10f1	$\times\vert\times$	1.797|1.899	303.4|261.3	3.99|4.14	23.71|21.04
AD10f2	$\times\vert\times$	1.901|1.980	272.4|245.2	4.15|5.91	21.07|19.30
AD10f3	$\times\vert\bullet$	1.984|2.042	261.2|239.3	5.52|6.39	20.40|18.53
AD10f4	$\bullet\vert\bullet$	2.096|2.098	249.8|231.7	7.32|6.67	18.70|17.83
AD11f2	$\times\vert\times$	1.734|1.845	296.9|257.6	3.78|4.13	24.23|21.65
AD12f3	$\times\vert\times$	0.319|1.555	372.3|249.4	1.61|4.08	22.88|23.08
AD12f4	$\times\vert\times$	1.432|1.677	298.1|257.9	3.14|4.44	24.58|22.97
AD13f4	$\times\vert\times$	7×10^{-4}|0.312	331.8|322.9	0.40|2.01	15.39|24.02

[45,103]. The 10% scaling yields values in between those of [28,45,103] and, hence, allows us to study trends in AIC dynamics with variations in deleptonization in between constraints provided by simulations. We will not list the results of these tests in our summary tables, but discuss them wherever the context requires their consideration (i.e., Secs. III A, III B, and IV).

D. Gravitational-wave extraction

We employ the Newtonian quadrupole formula in the first moment of momentum density formulation as discussed, e.g., in [80,83,104]. In essence, we compute the quadrupole wave amplitude $A_{20}^{\rm E2}$ of the $l = 2$, $m = 0$ mode in a multipole expansion of the radiation field into pure-spin tensor harmonics [105]. In axisymmetric AIC, this quadrupole mode provides by far the largest contribution to the GW emission, and other modes are at least one or more orders of magnitude smaller. Of course, should nonaxisymmetric instabilities develop (which we cannot track in our current 2D models), these would then provide a considerable nonaxisymmetric contribution to the GW signal.

The GW amplitude is related to the dimensionless GW strain h in the equatorial plane by

$$h = \frac{1}{8}\sqrt{\frac{15}{\pi}}\left(\frac{A_{20}^{\rm E2}}{r}\right) = 8.8524 \times 10^{-21}\left(\frac{A_{20}^{\rm E2}}{10^3\ {\rm cm}}\right)\left(\frac{10\ {\rm kpc}}{r}\right), \tag{12}$$

where r is the distance to the emitting source.

We point out that although the quadrupole formula is not gauge invariant and is only valid in the weak-field slow-motion limit, it yields results that agree very well in phase and to ~10%–20% in amplitude with more sophisticated methods [104,106,107].

In order to assess the prospects for detection by current and planned interferometric detectors, we calculate characteristic quantities for the GW signal following [40]. Performing a Fourier transform of the dimensionless GW strain h,

$$\hat{h} = \int_{-\infty}^{\infty} e^{2\pi i f t} h dt, \tag{13}$$

we can compute the (detector-dependent) integrated characteristic frequency

$$f_{\rm c} = \left(\int_0^{\infty} \frac{\langle \hat{h}^2 \rangle}{S_h} f df\right)\left(\int_0^{\infty} \frac{\langle \hat{h}^2 \rangle}{S_h} df\right)^{-1}, \tag{14}$$

and the dimensionless integrated characteristic strain

$$h_{\rm c} = \left(3 \int_0^{\infty} \frac{S_{h,{\rm c}}}{S_h} \langle \hat{h}^2 \rangle f df\right)^{1/2}, \tag{15}$$

where S_h is the power spectral density of the detector and $S_{h,{\rm c}} = S_h(f_{\rm c})$. We approximate the average $\langle \hat{h}^2 \rangle$ over randomly distributed angles by $(3/2)\hat{h}^2$. From Eqs. (14) and (15) the optimal single-detector signal-to-noise ratio (SNR) can be calculated as

$$\text{SNR} \equiv \frac{h_{\rm c}}{h_{\rm rms}(f_{\rm c})}, \tag{16}$$

where $h_{\rm rms} = \sqrt{f S_h}$ is the value of the root-mean-square strain noise for the detector.

III. COLLAPSE DYNAMICS

The AIC starts when the progenitor WD reaches its effective Chandrasekhar mass and pressure support is reduced due to electron capture in the core. Similar to the case of massive star iron core collapse (e.g., [76,83,108,109] and references therein), the collapse evolution can be divided into three phases:

Infall. This is the longest phase of collapse and, depending on model parameters, lasts between ~25 ms and ~300 ms. The inner part of the WD core (the "inner core"), which is in sonic contact, contracts homologously ($v_r \propto r$), while the "outer core" collapses supersonically. Figure 7 shows the time evolution of the central density for the nonrotating high-T AIC models. In the infall phase, the core contracts slowly, which is reflected in the slow increase of $\rho_{\rm c}$.

Plunge and bounce. The short dynamical "plunge" phase sets in when $\rho_{\rm c}$ reaches ~10^{12} g cm^{-3}, and the

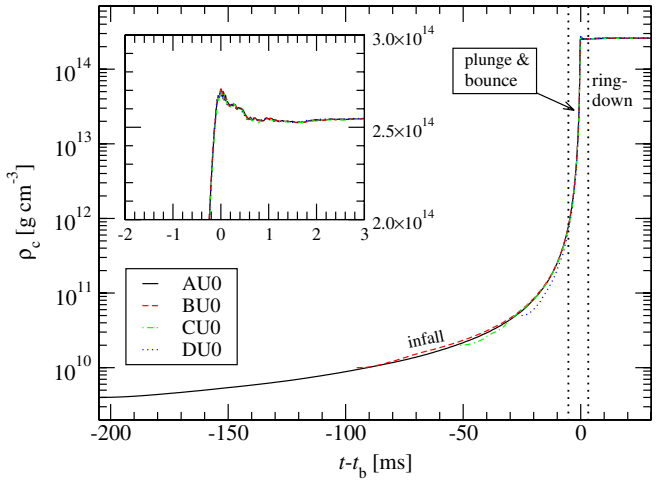

FIG. 7 (color online). Evolution of the maximum (central) density for the nonrotating low-T models AU0, BU0, CU0, and DU0. The inset plot displays a zoomed-in view of the maximum density around the time of core bounce on a linear scale. As is clearly discernible from this figure, the collapse dynamics in the plunge and bounce phase are essentially independent of the initial WD central density. Time is normalized to the time of bounce $t_{\rm b}$.

peak radial infall velocity is $\sim 0.1c$. At this point, neutrinos begin to be trapped in the inner core. The latter rapidly contracts to reach nuclear densities ($\rho_{\rm nuc} \simeq 2.7 \times 10^{14}$ g cm^{-3}) at which the nuclear EOS stiffens, decelerating and eventually reversing the infall of the inner core on a millisecond time scale. Because of its large inertia and kinetic energy, the inner core does not come to rest immediately. It overshoots its equilibrium configuration, then bounces back, launching a shock wave at its outer edge into the still infalling outer core. The bounce and the reexpansion of the inner core is also evident in the time evolution of $\rho_{\rm c}$ shown in Fig. 7 which, at core bounce, reaches a value of $\sim 2.8 \times 10^{14}$ g cm^{-3} in the nonrotating AIC models, after which the core slightly reexpands and settles down at $\sim 2.5 \times 10^{14}$ g cm^{-3}. As pointed out by extensive previous work (see, e.g., [8,50,110–112] and references therein), the extent of the inner core at bounce determines the initial kinetic energy imparted to the bounce shock, the mass cut for the material that remains to be dissociated, and the amount of angular momentum that may become dynamically relevant at bounce.

Ringdown. Following bounce, the inner core oscillates with a superposition of various damped oscillation modes with frequencies in the range of 500–800 Hz, exhibiting weak low-amplitude variations in $\rho_{\rm c}$ (Fig. 7). These oscillations experience rapid damping on a time scale of 10 ms due to the emission of strong sound waves into the postshock region which steepen into shocks. The newly born PNS thus rings down to its new equilibrium state.

The ringdown phase is coincident with the burst of neutrinos that is emitted when the bounce shock breaks out of the energy-dependent neutrinospheres (see, e.g., [28,91]). The neutrino burst removes energy from the postshock regions and enhances the damping of the PNS ringdown oscillations (e.g., [53]), but, due to the limitations of our present scheme (see Sec. II A 2), is not accounted for in our models.

A. Nonrotating AIC

The set of nonrotating AIC models that we consider here consists of models AU0, BU0, CU0, DU0. As noted in Sec. II C 1, these models have different central densities with values in the range from 4×10^9 to 5×10^{10} g cm^{-3} which, because of the strong dependence of the WD compactness on the central density, corresponds to a range of WD radii from 1692 to 813 km (see Fig. 2). Once mapped onto our computational grid and after the initial $\bar{Y}_e(\rho)$ parametrization is applied (see Sec. II B 4), all WD models start to collapse by themselves and no additional artificial pressure reduction is necessary. This is in contrast to previous work that employed a simple analytic EOS and required an explicit and global change of the adiabatic exponent to initiate collapse (e.g., [76,78]).

The free-fall collapse time $\tau_{\rm ff}$ of a Newtonian self-gravitating object of mean density $\rho_{\rm mean}$ is proportional to $\rho_{\rm mean}^{-1/2}$. For our set of spherically symmetric AIC models we find a scaling $\tau_{\rm ff} \propto \rho_{\rm c}^{-0.87}$, where $\rho_{\rm c}$ is the precollapse central density of the WD. This stronger scaling is due to the fact that WD cores are not constant density objects and that the collapse is not pressureless. Furthermore, the pressure reduction initiating and accelerating collapse is due primarily to electron capture which scales roughly with $\rho^{5/3}$ (e.g., [8]). Hence, lower-density WDs collapse only slowly, spending much of their collapse time near their initial equilibrium states.

In Fig. 7, we plot the evolution of the central densities of the nonrotating high-T models. Despite the strong dependence of the collapse times on the initial central densities, the evolution of $\rho_{\rm c}$ around bounce does not exhibit a dependence on the initial central density. Moreover, the mass and the size of the inner core is rather insensitive to the initial value of $\rho_{\rm c}$.

These features, somewhat surprising in the light of the strong dependence of the collapse times on the initial value of $\rho_{\rm c}$, are a consequence of the fact that the inner-core mass is determined primarily not by hydrodynamics, but by the thermodynamic and compositional structure of the inner core set by nuclear and neutrino physics [8]. However, an important role is played also by the fact that an increase (decrease) of the central density of an equilibrium WD leads to a practically exact homologous[3] contraction (expansion) of the WD structure in the inner regions [$m(\varpi) \lesssim 1 M_\odot$] in the nonrotating case (this can be seen in Fig. 11), at least in the range of central densities considered in this paper (as we shall see in Sec. III B, this feature also holds to good accuracy in the case of rotating WDs). These aspects, in combination with the homologous nature of WD inner-core collapse, make the size and dynamics of the inner core in the bounce phase practically independent of the central density of the initial equilibrium WDs. Early analytical work [8,110,111] demonstrated (neglecting thermal corrections [114] and rotation) that the mass $M_{\rm ic}$ of the inner core is proportional to Y_e^2 in the infall phase during which the fluid pressure is dominated by the contribution of degenerate electrons. Around bounce, at densities near nuclear matter density, the nuclear component dominates and the simple Y_e^2 dependence does not hold exactly any longer. As discussed in Sec. II B 4, we adopt the parametrization $\bar{Y}_e(\rho)$ as extracted from the simulations of Dessart *et al.* [28] which predict very efficient electron capture, resulting in an average inner-core Y_e at bounce of ~ 0.18 in the high-T models. This is significantly lower than in standard iron core collapse where the inner-core Y_e at bounce is expected to be around ~ 0.25–0.30 [91,94,115]. In our nonrotating AIC models, we find inner-core masses at

[3]For a discussion of homology in the stellar structure context, see [113].

bounce $M_{\rm ic,b} \sim 0.27 M_\odot$[4] (see Fig. 13) which are, as expected, significantly smaller than in iron core collapse (where $M_{\rm ic,b} \sim 0.5 M_\odot$ [94,115,116]). Because of their small mass, our AIC inner cores have less kinetic energy at bounce and reach lower densities than their iron-core counterparts. For example, the nonrotating AIC models exhibit central densities at bounce of $\sim 2.8 \times 10^{14}$ g cm^{-3}, while in nonrotating iron core collapse, maximum densities of $\gtrsim 3 \times 10^{14}$ g cm^{-3} are generally reached at bounce in simulations (e.g., [50]). In addition to $M_{\rm ic,b}$, the bounce density depends also on the stiffness of the nuclear EOS whose variation we do not explore here (see, e.g., [50,117]).

Since the free proton fraction at precollapse and early collapse densities grows rather rapidly with temperature in the range from $\sim 10^9$ to $\sim 10^{10}$ K (e.g., [118]), the efficiency of electron capture is sensitive to the temperature of WD matter. For example, in the low-T models, the value of Y_e drops to $\simeq 0.32$ when the density reaches 10^{12} g cm^{-3}, while in the high-T models, we obtain $Y_e \simeq 0.3$ at that time. Because of this dependence of Y_e on T, the inner core masses of low-T models are larger by $\sim 10\%$ compared to those of high-T models. Moreover, since the electron degeneracy pressure is proportional to $(Y_e \rho)^{4/3}$ [8], the collapse times of the low-T models are longer by $\sim 5\%$. We find similar systematics in test calculations in which we modify the $\bar{Y}_e(\rho)$ trajectories of low-T models to yield larger Y_e at bounce (see Sec. II C 3). An increase of the inner-core Y_e by 10% (20%) leads to an increase of $M_{\rm ic,b}$ by $\sim 11\%$ ($\sim 25\%$).

It is important to note that the nonrotating AIC models discussed above, as well as all of the other models considered in this study, experience prompt hydrodynamic explosions. The bounce shock, once formed, does slow down, but never stalls and steadily propagates outwards. While the shock propagation is insensitive to the initial WD temperature profile, it shows significant dependence on the initial WD central density: Owing to the greater initial compactness and the steeper density gradient of the higher-density models, the shock propagation in those models is faster and the shock remains stronger when it reaches the WD surface. For example, in the lowest-density progenitor model AU0, the shock reaches the surface within ~ 120 ms after its formation, while in the highest-density model DU0, it needs only ~ 80 ms. We point out that Dessart *et al.* [28,29] and previous AIC studies [26,27] reported significant shock stagnation in the postbounce phase of AIC due to the dissociation of infalling material and neutrino losses from the postshock region. Our present computational approach includes dissociation (through the EOS, see Sec. II A 1), but does not account for neutrino losses in the postbounce phase. Hence, the ''prompt'' explosions in our models are most likely an artifact of our incomplete treatment of the postbounce physics.

B. Rotating AIC

The AIC of rotating models proceeds through the same stages as AIC without rotation and exhibits similar general features, including the well defined split of the WD into an inner core that is in sonic contact and collapses quasihomologously,[5] and a supersonically infalling outer core. Conservation of angular momentum leads to an increase of the angular velocity $\Omega \propto \varpi^{-2}$ and of the centrifugal acceleration $a_{\rm cent} = \Omega^2 \varpi \propto \varpi^{-3}$. The latter has an opposite sign to gravitational acceleration, and hence provides increasing centrifugal support during collapse, slowing down the contraction and, if sufficiently strong, leading to centrifugally induced core bounce only slightly above nuclear density or even at subnuclear density [109,119].

Just as in the case of nonrotating AIC, models of set A collapse more slowly than D models because of the dependence of the collapse times on the initial central densities. However, due to centrifugal support, the collapse times grow with increasing precollapse rotation. This is visualized in Fig. 8 in which we plot the time to core bounce as a function of the initial central angular velocity $\Omega_{\rm c,i}$. The maximum angular velocity of uniformly rotating models is limited by the WD surface mass-shedding limit and is ~ 3.5 rad s^{-1} (~ 9.5 rad s^{-1}) in model AU5 (DU7). The effect of rotation on the collapse time of uniformly rotating models) is small, and the time to core bounce increases by $\sim 5\%$ from zero to maximum precollapse rotation in model set A. The more compact D models collapse much faster than their lower initial density A counterparts and, in addition, experience a smaller spin-up of their more compact inner cores. Hence, uniformly rotating D models are less affected by rotation and their collapse times vary by only $\sim 0.8\%$ from zero to maximum rotation.

As mentioned in Sec. II B 2, WD models that rotate differentially according to the rotation law of Yoon and Langer [7,23] have an angular velocity that increases from its central value $\Omega_{\rm c,i}$ with ϖ up to a maximum $\Omega_{\rm max,i}$ at the cylindrical radius $\varpi_{\rm p}$, beyond which Ω decreases to sub-Keplerian values at the surface (see Fig. 3). The rate at which Ω increases in the WD core is controlled by the

[4]We define the inner core as the region which is in sonic contact at the time of bounce, i.e.,

$$M_{\rm ic,b} \equiv \int_{|v_r|<c_s} \rho W dV, \tag{17}$$

where W is the Lorentz factor and dV is the invariant 3-volume element. The bounce time is defined as the time when the radial velocity of the outer edge of the inner core becomes positive. Note that such a measure of the inner core is strictly valid only at the time of bounce.

[5]The collapse is *quasi*homologous because in this case the relation between the infall velocity v_r depends on both the radial coordinate and on the polar coordinate [76].

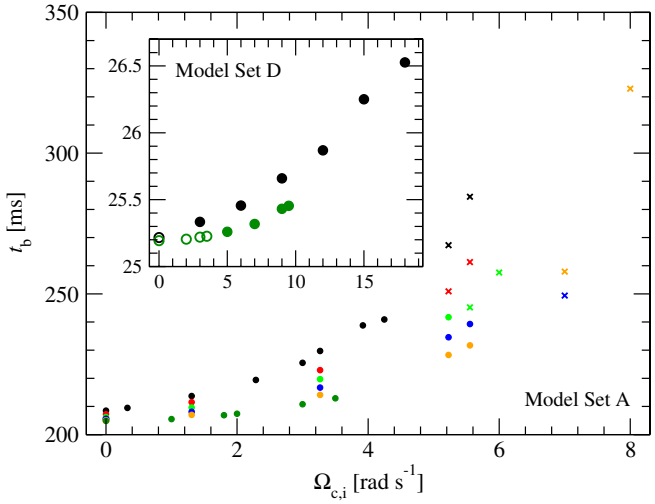

FIG. 8 (color online). Times to core bounce from the onset of collapse as a function of initial central angular velocity $\Omega_{c,i}$. Shown are the results of the high-T model sequence (the low-T models exhibit identical systematics). Models denoted by an unfilled (filled) circle undergo a pressure-dominated bounce with (without) significant prompt postbounce convection. Models marked by a cross undergo centrifugal bounce at subnuclear densities, and models marked with a small (large) symbol are of set A (D). The colors correspond to various precollapse rotational configurations (see the legend in Fig. 9). Note that due to their much higher initial compactness, the high-density D models (shown in the inset plot) have much shorter collapse times than their lower-density A counterparts.

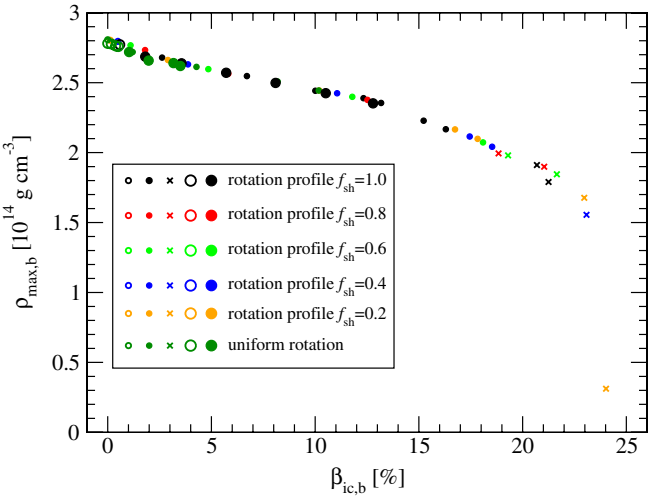

FIG. 9 (color online). The maximum density $\rho_{max,b}$ at bounce as a function of the inner-core parameter $\beta_{ic,b}$ at bounce for the entire set of high-T AIC models. Because of the increasing role of centrifugal support, $\rho_{max,b}$ decreases monotonically with increasing rotation (see the main text for details). The symbol convention for the various sets is explained in the caption of Fig. 8.

shear parameter f_{sh}, which we choose in the range from 0.2 to 1. The case $f_{sh} = 0.2$ corresponds to a nearly uniformly rotating inner region, while $f_{sh} = 1$ corresponds to strong differential rotation with $\Omega(\varpi_p)/\Omega_{c,i} \sim 2$–3. In mass coordinate, this corresponds to a ratio $\Omega(M_{ic,b})/\Omega_{c,i}$ of $\sim$1.4–2.4, where $M_{ic,b} \simeq 0.3 M_\odot$ is the approximate mass that constitutes the inner core at bounce in a nonrotating WD model.

In contrast to uniformly rotating models, differentially rotating WDs are not limited by the mass-shedding limit at the surface. As a result, $\Omega_{c,i}$ can in principle be increased up to the point beyond which the precollapse WD inner core becomes fully centrifugally supported and does not collapse at all. For model set AD, this maximum of $\Omega_{c,i}$ is ~ 8 rad s^{-1} (the low-T model AD13f4, which becomes centrifugally supported already at a central density of $\sim 7 \times 10^{10}$ g cm^{-3}) while the more compact DD models still collapse rapidly at $\Omega_{c,i} \sim 18$ rad s^{-1} (model DD7). As shown in Fig. 8, the most rapidly rotating AD model (AD13f4) reaches core bounce after a time which is $\sim$55% larger than a nonrotating A model. For the most rapidly rotating DD model this difference is only $\sim$5%.

In Fig. 9 we plot the maximum density $\rho_{max,b}$ at bounce as a function of the inner-core parameter $\beta_{ic,b}$ at bounce. Slowly to moderately rapidly rotating WDs that reach $\beta_{ic,b} \lesssim 15\%$ are only mildly affected by rotation, and their $\rho_{max,b}$ decrease roughly linearly with increasing $\beta_{ic,b}$, but stay close to ρ_{nuc}. The effect of rotation becomes nonlinear in more rapidly rotating WDs. Models of our set that reach $\beta_{ic,b} \gtrsim 18\%$ (i.e., AD models with $\Omega_{c,i} \gtrsim 5$ rad s^{-1}) undergo core bounce induced partly or completely centrifugally at subnuclear densities.

As shown in Fig. 10, $\beta_{ic,b}$ is a monotonic function of $\Omega_{c,i}$, but is very sensitive to both the rotation law and the initial WD compactness. Our most rapidly uniformly rotating models AU5 and DU7 (both near the mass-shedding limit) reach $\beta_{ic,b}$ of $\sim$10.5% and $\sim$3.6%, respectively. Hence, uniformly rotating WDs always undergo core bounce due to the stiffening of the nuclear EOS and with little influence of rotation on the dynamics.

In models where centrifugal effects remain subdominant during collapse, $\beta_{ic,b}$ grows practically linearly with $\Omega_{c,i}$. This relationship flattens off for models that become partially or completely centrifugally supported near bounce. $\beta_{ic,b}$ grows with increasing rotation up to $\sim$24.5% (model AD13f4), beyond which any further increase in precollapse rotation leads to a decrease of $\beta_{ic,b}$, since the inner core becomes fully centrifugally supported before reaching high compactness and spin-up. In other words, there exists a "centrifugal limit" beyond which centrifugal forces dominate, and as a result, increasing precollapse rotation leads to a decreasing $\beta_{ic,b}$ at core bounce. This result is analogous to what previous studies [50,108] found in the rotating core collapse of massive stars and has consequences for the appearance of nonaxisymmetric rotational instabilities in PNSs. This will be discussed in more detail in Sec. V.

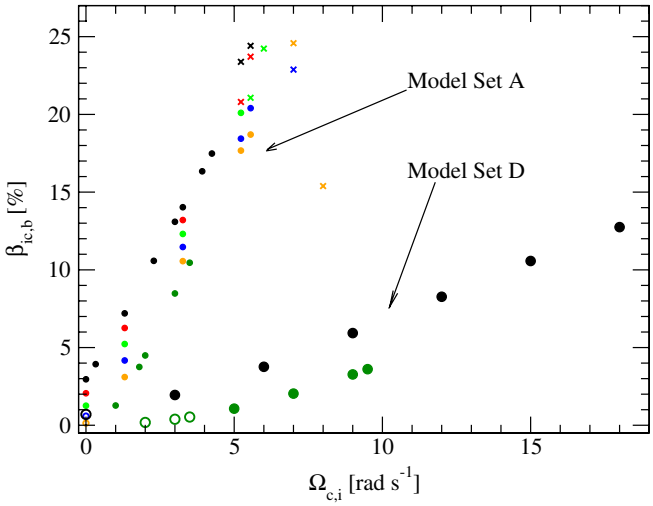

FIG. 10 (color online). The inner-core parameter $\beta_{ic,b}$ at the time of bounce for all low-T AIC models plotted as a function of the precollapse central angular velocity $\Omega_{c,i}$. For models with slow to moderately rapid rotation, $\beta_{ic,b}$ increases roughly linearly with $\Omega_{c,i}$ (at fixed $\rho_{c,i}$ and rotation law). In more rapidly rotating models, the growth of $\beta_{ic,b}$ saturates at $\sim$24.5%, and further increase of the progenitor rotation results in a decrease of $\beta_{ic,b}$. Since D models experience less spin-up during collapse than A models, an increase of $\rho_{c,i}$ at fixed $\Omega_{c,i}$ and rotation law results in a decrease of $\beta_{ic,b}$. A uniformly rotating model with a given $\Omega_{c,i}$ and $\rho_{c,i}$ reaches smaller $\beta_{ic,b}$ than the differentially rotating model with the same $\Omega_{c,i}$ and $\rho_{c,i}$. The symbol convention for the various sets is explained in the caption of Fig. 8.

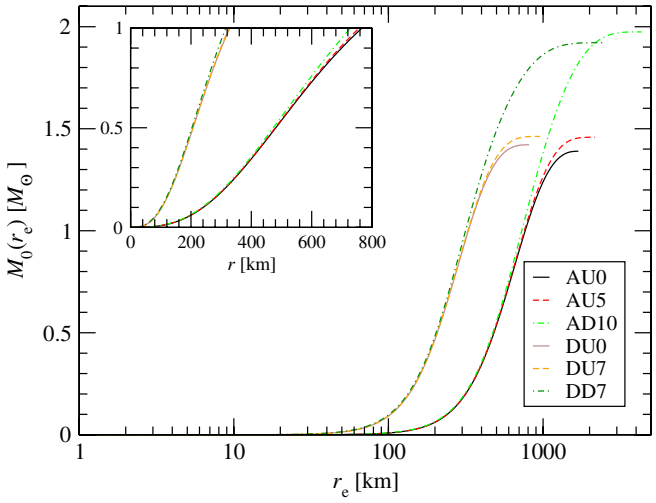

FIG. 11 (color online). Mass $M_0(r_e)$ in units of solar masses of the WD inner region plotted as a function of the equatorial radial coordinate r_e for a number of AIC models with slow and rapid rotation as well as high and small central densities. The inset plot shows the same on a linear radial scale. The mass distribution of the inner $M_0(r_e) \lesssim 0.5M_\odot$ region is largely independent of the rotational configuration, while an increase (decrease) of the central density leads to homologous contraction (expansion) of the inner regions. See Sec. II C for details of the model setups.

The influence of the precollapse compactness on the dynamics of rotating AIC can also easily be appreciated from Fig. 10. The higher-density, more compact WDs of set D spin up much less than their A counterparts since their inner cores are already very compact at the onset of collapse. Hence, a higher-density WD that reaches a given value of $\beta_{ic,b}$ must have started out with a larger $\Omega_{c,i}$ than a lower-density WD reaching the same $\beta_{ic,b}$. For the particular choice of initial central densities represented by D and A models and in the case of uniform or near-uniform rotation, the ratio between the $\Omega_{c,i}$ of a D and A model required to reach the same $\beta_{ic,b}$ is $\sim$5.3. This factor can be understood by considering Fig. 11 in which we plot the enclosed mass as a function of equatorial radial coordinate r_e of selected A and D initial WD configurations with slow and rapid rotation. The important thing to notice is that the WD core structure ($M \lesssim 0.5M_\odot$) is insensitive to the rotational configuration and obeys a homology relation. Stated differently, for a model of set D, a homologous expansion in the radial direction by a factor of $\sim$2.3 yields an object whose inner part is very similar to a lower-density A model. In turn, the collapse of A models corresponds to a $\sim$2.3 times greater contraction of the WD core compared to their D model counterparts and a spin-up that is greater by a factor of $\sim(2.3)^2 \simeq 5.3$. This explains the strong dependence of the inner-core angular velocity and $\beta_{ic,b}$ on the initial central density observed in Fig. 10. Furthermore, it suggests that one can find A–D model pairs that differ greatly in their precollapse angular velocities, but yield the same rotational configuration at bounce. An example for this is shown in Fig. 12 in which we plot for the uniformly rotating model pair AU2-DU7 the equatorial angular velocity profile at the time of bounce as well as the evolution of the central density around the time of bounce. AU2 and DU7 have practically identical angular velocity profiles and their core structure, core mass, and $\beta_{ic,b}$ agree very closely. As can be seen in the inset plot of Fig. 12, this results in nearly identical ρ_c time evolutions around bounce and demonstrates that WDs with quite different precollapse structure and rotational setup can produce identical bounce and postbounce dynamics. This can also occur for pairs of differentially rotating models and is an important aspect to keep in mind when interpreting the GW signal from AIC discussed in Sec. IV.

Figure 13 shows the mapping between $\beta_{ic,b}$ and the inner-core mass $M_{ic,b}$ at bounce for all high-T models. Rapid (differential) rotation not only increases the equilibrium mass of WDs (see Table I), but rotational support also increases the extent of the region in sonic contact during collapse. Hence, it may be expected that $M_{ic,b}$ grows with increasing rotation. However, for WDs below $\beta_{ic,b} \lesssim 13\%$, $M_{ic,b}$ is essentially unaffected by rotation and stays within $0.02M_\odot$ of the nonrotating value of $0.28M_\odot$. Only when the effects of rotation become strong at $\beta_{ic,b} \gtrsim 13\%$–$18\%$ does $M_{ic,b}$ increase roughly linearly with $\beta_{ic,b}$. WDs that

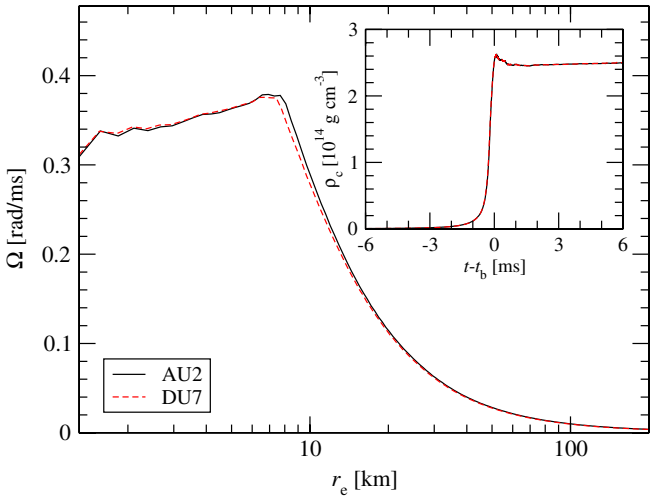

FIG. 12 (color online). Angular velocity profiles in the equatorial plane at the time of core bounce and time evolution of the central density ρ_c (in the inset) for models AU2 and DU7. The initial angular velocity of model DU7 is larger by a factor of ~5.3 than that of model AU2, but the latter experiences a ~5.3 greater spin-up during collapse. As a result, these models produce inner cores with almost identical rotational configurations and similar masses in the bounce phase. This is reflected in an identical evolution of the central densities at bounce.

undergo centrifugal bounce have $\beta_{ic,b} \gtrsim 18\%$ and correspondingly large inner cores that are more massive than $\sim 0.5 M_\odot$. Such values of $M_{ic,b}$ are accessible only to differentially rotating WDs.

Also for rotating models, the dependence of the AIC dynamics on the initial temperature of AIC progenitor WDs is simple and straightforwardly understood from

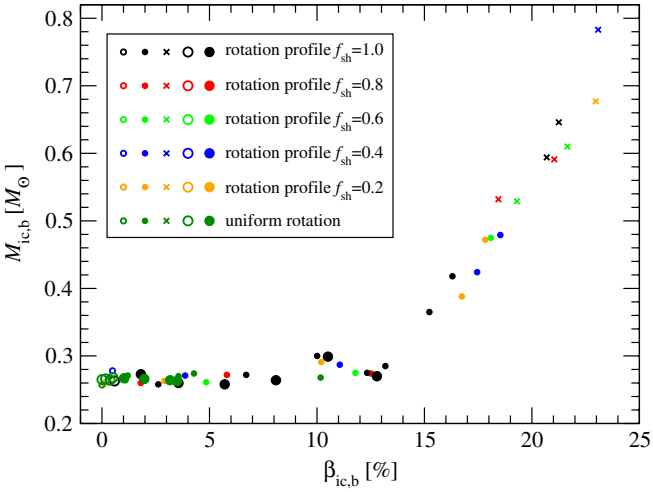

FIG. 13 (color online). Mass $M_{ic,b}$ of the inner core at bounce for all high-T models versus the parameter $\beta_{ic,b}$ of the inner core at bounce. The systematics of $M_{ic,b}$ with $\beta_{ic,b}$ are identical for the set of low-T models, but their $M_{ic,b}$ are generally ~10% larger. The symbol convention for the various sets is explained in the caption of Fig. 8.

the nonrotating results discussed in Sec. III A. These show that the low-T models yield inner cores that are ~10% larger in mass than in their twice-as-hot high-T counterparts. Because of their larger mass, the inner cores of collapsing low-T AIC progenitors also contain a larger amount of angular momentum. At fixed rotation law and $\Omega_{c,i}$, they reach values of $\beta_{ic,b}$ that are larger by up to ~5% (in absolute value). Hence, lower-T WDs become affected by centrifugal support, bounce centrifugally, and reach the centrifugal limit at lower $\Omega_{c,i}$ than their higher-T counterparts. Along the same lines behave test calculations in which we impose increased inner-core values of Y_e (see Secs. II A 2 and II C 3). The increased Y_e leads to more massive and more extended inner cores which, in turn, are more likely to experience a centrifugal support.

To conclude our discussion of rotating AIC, we summarize for the reader that the PNSs born from the set of differentially (uniformly) rotating AIC models considered here have average angular velocities[6] in the range from 0 to ~5 rad ms^{-1} (~ 3.3 rad ms^{-1}), while their pole to equator axis ratios vary from 1 to ~0.4 (~ 0.6).[7] Some of the rapidly rotating WDs produce PNSs with a slightly off-center maximum in density, though the density distribution of the inner regions does not exhibit a pronounced toroidal geometry. The clearest deviation from a centrally peaked density distribution is produced in the case of model AD10, which reaches $\beta_{ic,b} \simeq 21.3\%$ ($\beta_{ic,b} \simeq 24.4\%$) in its high-$T$ (low-T) variant. In this model, the point of highest density after bounce is located at $r \simeq 0.94$ km, but the maximum value is larger than the central density value by only ~0.3%. For models with less rapid rotation, the off-center maximum is much less pronounced, and completely disappears for $\beta_{ic,b}$ below ~20%.

C. Shock propagation and the formation of quasikeplerian disks

As pointed out earlier (see Sec. III A), all AIC models considered in this study undergo weak hydrodynamic explosions. This is an artifact of our approach that neglects postbounce neutrino emission, but is unlikely to strongly affect the results presented in this section, since in the MGFLD simulations of [28], the shock stalls only for a very short period and a weak explosion is quickly initiated by neutrino heating.

In moderately rapidly and rapidly rotating AIC (with $\beta_{ic,b} \gtrsim 5\%$), the shock propagation is significantly af-

[6]The average angular velocity $\bar{\Omega}$ of the differentially rotating models considered here is computed using the approximation $\bar{\Omega} = J_{ic}/I_{ic}$, where J_{ic} is the inner-core angular momentum and I_{ic} is the (Newtonian) inner-core moment of inertia.

[7]The PNS formed in the AIC of WDs is surrounded by hot low-density material in the early postbounce phase, making it hard to define the boundary of the PNS unambiguously. For the present rough estimate of the axis ratio, we assume a density threshold of 10^{12} g cm^{-3} to mark the boundary of the PNS.

fected by centrifugal effects. The material near the equatorial plane of rotating WDs experiences considerable centrifugal support, and its collapse dynamics is slowed down. As a consequence, the bounce is less violent and the bounce shock starts out weaker near the equatorial plane than along the poles. Centrifugal support of low-latitude material also leads to reduced postbounce mass accretion rates near the equatorial plane, facilitating steady propagation of the shock at low latitudes. In the polar direction, where centrifugal support is absent, the shock propagates even faster due to the steeper density gradient and smaller polar radius of the WD. This quickly leads to a prolate deformation of the shock front in all rotating models, and the shock hits the polar WD surface much before it breaks out of the equatorial envelope. This is shown in Fig. 14, where we plot the equatorial and polar profiles of the radial velocity and specific entropy per baryon for model DD7 at various postbounce times. Because of the prolateness of the shock front, it breaks out of the polar surface ~130 ms before reaching the WD's equatorial surface. Moreover, due to the anisotropy of the density gradient and the initial shock strength, the specific entropy of the shock-heated material is larger by a factor of ~2–3 along the polar direction.

The asphericity of the shock front and the anisotropy of the shock strength become more pronounced in AIC with increasing rotation [53,78]. As pointed out in Sec. III A, due to the their greater initial compactness and thus steeper density gradients, the shock propagates faster in D models: In model DD1, for example, the shock reaches the surface in the equatorial plane within ~88 ms, while for model AD1, the corresponding time is ~143 ms.

Rapid rotation, and, in particular, rapid differential rotation, increases the maximum allowable WD mass. The most rapidly uniformly rotating WDs in our model set (i.e., models DU7 and AU5) have an equilibrium mass of $\sim 1.46 M_\odot$, which is only slightly above $M_{\rm Ch}$ in the nonrotating limit. Our most rapidly differentially rotating WDs (models AD13f2 and DD7), on the other hand, reach equilibrium masses of up to $\sim 2 M_\odot$. Much of the rotation-

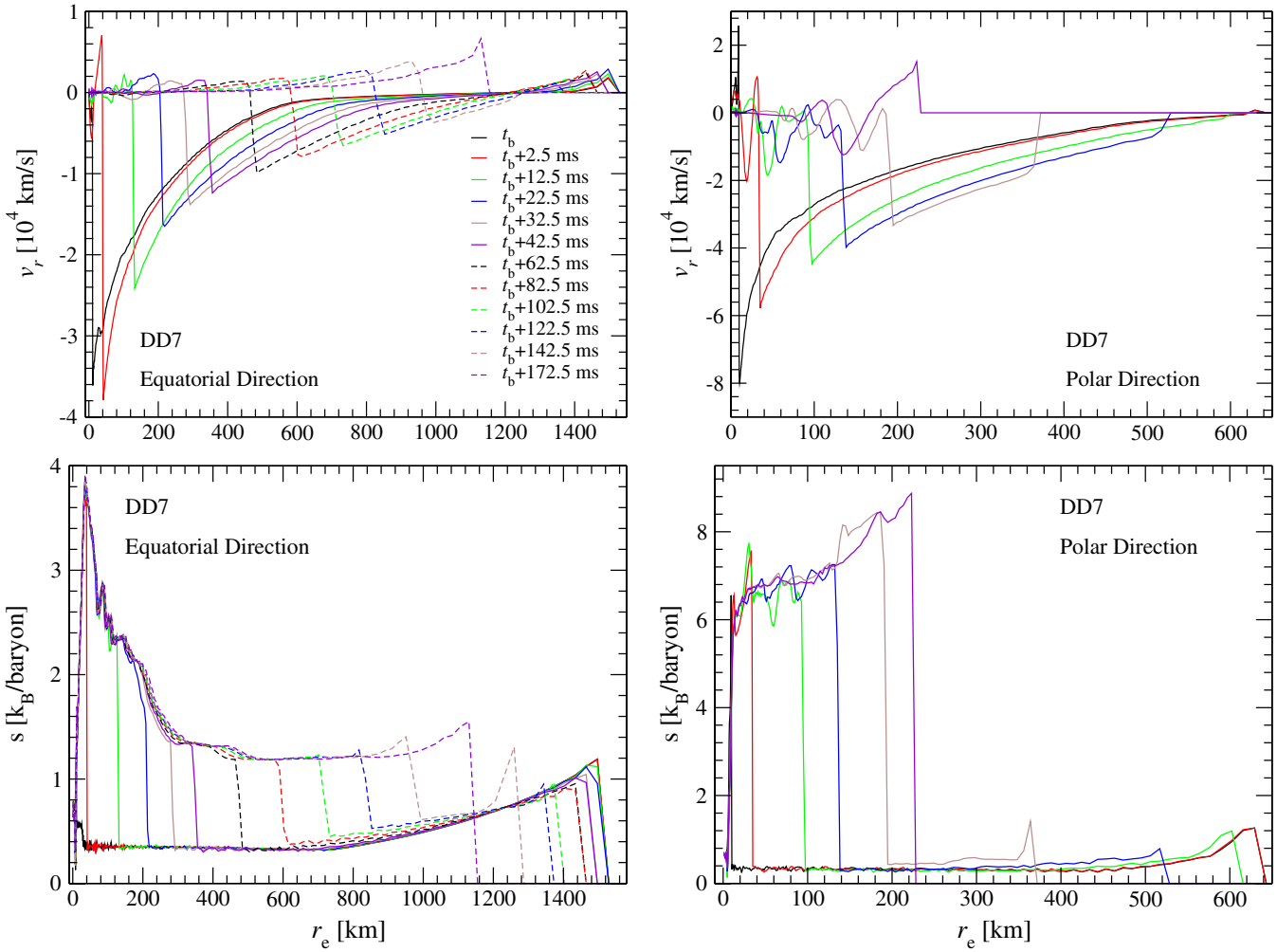

FIG. 14 (color online). Profiles of radial velocity (top panels) and specific entropy per baryon (bottom panels) at different postbounce times for AIC model DD7.

ally supported material is situated at low latitudes in the outer WD core, falls in only slightly during collapse, and forms a quasi-Keplerian disklike structure. The equatorial bounce shock is not sufficiently strong to eject much of the disk material and "wraps" around the disk structure, producing only a small outflow of outer disk material at $v_r \lesssim 0.025c$. This is in agreement with Dessart *et al.* [28], who first pointed out that rapidly rotating AIC produces PNSs surrounded by massive quasi-Keplerian disklike structures in the early postbounce phase. As recently investigated by Metzger, Piro, and Quataert [49] (but not simulated here), the hot disk will experience neutrino cooling on a time scale of $\sim$0.1 s, driving the disk composition neutron-rich to reach $Y_e \sim 0.1$ [28,49], depleting the pressure support and leading to limited contraction of the inner parts of the disk. The outer and higher-latitude regions expand with a neutrino-driven wind [28]. As discussed by [49], subsequent irradiation of the disk by neutrinos from the PNS increases its proton-to-neutron ratio, and Y_e may reach values as high as $\sim$0.5 by the time the weak interactions in the disk freeze out. The disk becomes radiatively inefficient, α particles begin to recombine, and a powerful disk wind develops, blowing off most of the disk's remaining material. Metzger, Piro, and Quataert [49] argue that, depending on disk mass, the outflows synthesize of the order of 10^{-3}–$10^{-2} M_\odot$ of ^{56}Ni, but very small amounts of intermediate-mass isotopes, making such AIC explosions spectroscopically distinct from ^{56}Ni outflows in standard core-collapse and thermonuclear SNe.

Our results, summarized in Table III, show that the masses and the geometry of the disks produced in AIC are sensitive to the angular momentum distribution in the precollapse WDs. In models with uniform rotation below the mass-shedding limit, only a very small amount of low-latitude material rotates at near-Keplerian angular velocities. Therefore, most of the outer-core material of such models undergoes significant infall, so that uniformly rotating WDs will generally produce small disks. The largest disk mass for uniform rotation is $M_{\rm disk} \sim 0.03 M_\odot$[8] and is produced in model AU5 which rotates near the mass-shedding limit. Since the angular velocity of the outer ($\varpi > \varpi_{\rm p}$) core of differentially rotating models is set to reach nearly Keplerian values [cf. Eq. (9)], most of the outer WD envelope has substantial centrifugal support and thus the differentially rotating models yield significantly larger $M_{\rm disk}$. For example, model AD4 which has $\beta_{\rm ic,b}$ and total angular momentum comparable to model AU5 yields a disk mass of $\sim 0.2 M_\odot$.

TABLE III. Summary of properties of the quasi-Keplerian disks formed in the set of AIC models AD, AU, DD, and DU. $H_{\rm disk}$ is the thickness and $R_{\rm e}$ is the equatorial radius of the disk, while $M_{\rm disk}$ is its mass. These quantities are computed at the time when the shock reaches the WD surface in the equatorial plane. The disk parameters do not vary significantly between the two choices of WD temperature considered in this study.

Collapse model	$R_{\rm e}$ [km]	$H_{\rm disk}/R_{\rm e}$	$M_{\rm disk}$ [$M_\odot$]
AU1	347	0.928	$\lesssim 10^{-3}$
AU2	401	0.903	$\lesssim 10^{-3}$
AU3	447	0.848	$\lesssim 10^{-3}$
AU4	732	0.577	0.002
AU5	907	0.484	0.030
DU1	248	0.980	$\lesssim 10^{-3}$
DU2	249	0.971	$\lesssim 10^{-3}$
DU3	249	0.952	$\lesssim 10^{-3}$
DU4	261	0.916	$\lesssim 10^{-3}$
DU5	291	0.801	$\lesssim 10^{-3}$
DU6	332	0.701	$\lesssim 10^{-3}$
DU7	350	0.671	0.007
AD1	866	0.479	0.030
AD2	935	0.452	0.038
AD3	1118	0.437	0.093
AD4	1321	0.410	0.222
AD5	1558	0.374	0.323
AD6	1638	0.370	0.356
AD7	1784	0.377	0.470
AD8	1912	0.382	0.507
AD9	2278	0.342	0.607
AD10	2700	0.296	0.805
DD1	360	0.669	0.005
DD2	402	0.597	0.008
DD3	461	0.525	0.019
DD4	554	0.466	0.054
DD5	670	0.436	0.161
DD6	853	0.374	0.279
DD7	1313	0.255	0.507

The total mass of the disk and its equatorial radius (the disk thickness $H_{\rm disk}$) grow with increasing rotation (see Table III). Slowly rotating models such as AD1 have little centrifugally supported material and acquire spheroidal shape soon after bounce, resulting in a disk mass as small as $\sim 0.03 M_\odot$. More rapidly rotating models such as AD10 produce significantly more strongly flattened disks, with $R_{\rm e} \sim 2700$ km, $H_{\rm disk} \sim 800$ km, and a disk mass $M_{\rm disk}$ of $\sim 0.8 M_\odot$. Because of the greater initial compactness of the higher-density D models, their disks are less massive and have smaller equatorial radii when compared to A models. Hence, when considering two WDs of set A and D with the same total angular momentum, the mass and equatorial extent of the disk in the D model will be smaller by a factor of $\sim$1.5–2.

[8]We point out that because the disks do not settle down to exact equilibrium right after bounce or not even after shock passage, it is hard to introduce an unambiguous definition of the disk mass. In the present study, we define the disk as the structure that surrounds the PNS at $\varpi > 20$ km with densities below 10^{11} g cm^{-3} and angular velocity $\Omega > 0.58\Omega_{\rm K}$. The latter condition ensures that the disk cannot contract by more than a factor of $\sim$3 as a result of cooling.

These results indicate that massive disks of $M_{\rm disk} \gtrsim 0.1 M_\odot$ are unlikely to be compatible with the assumption of uniformly rotating accreting WDs argued for by [22,102]. In order to produce disks of appreciable mass and significant ^{56}Ni outflows in AIC, the progenitor either must be an accreting WD obeying a differential rotation law similar to that proposed by [7,23] or may be the remnant of a binary-WD merger event. However, for the latter, the differential rotation law is unknown and may be very different from what we consider here (for a discussion of binary-WD merger simulations, see, e.g., [120] and references therein).

IV. GRAVITATIONAL-WAVE EMISSION

In Fig. 15, we present the time evolution of the GW strain h at an assumed source distance of 10 kpc for a representative set of AIC models evolved with the $\bar{Y}_e(\rho)$ parametrization obtained from [28]. The GW signals of all models have the same overall morphology. This general AIC GW signal shape bears strong resemblance to GW signals that have been classified as "type III" in the past [42,76,78], but also has features in common with the GW signals predicted for rotating iron core collapse ("type I," [50]).

The GW strain h in our AIC models is positive in the infall phase and increases monotonically with time, reaching its peak value in the plunge phase, just $\sim$0.1 ms before bounce. Then, h rapidly decreases, reaching a negative peak value within $\sim$1–2 ms. While the first positive peak is produced by rapid infall of the inner core, the first negative peak is caused by the reversal of the infall velocities at bounce. Following the large negative peak, h oscillates with smaller amplitude with a damping time of $\sim$10 ms, reflecting the hydrodynamical ringdown oscillations of the PNS. Although all AIC models of our base line set produce type III signals, we can introduce three subtypes whose individual occurrence depends on the parameter $\beta_{\rm ic,b}$ of the inner core at bounce:

Type IIIa. In slowly rotating WDs (that reach $\beta_{\rm ic,b} \lesssim 0.7\%$), strong prompt convective overturn develops in the early postbounce phase, adding a lower-frequency contribution to the regular ringdown signal (e.g., models AD1f4, DU3). The largest-amplitude part of this GW signal type comes from the prompt convection. Nevertheless, the GW signal produced by the bouncing centrifugally deformed inner core is still discernible, with the first positive peak being generally larger by a factor of $\sim$2 than the first negative peak. Subsequent ringdown peaks are smaller by a factor of $\gtrsim 3$. We point out that the observed prompt postbounce convection is most likely overestimated in our approach, since we do not take into account neutrino losses and energy deposition by neutrinos in the immediate postshock region, whose effect will quickly smooth out the negative entropy gradient left behind by the shock and thus significantly damp this early convective instability in full postbounce radiation-hydrodynamics calculations (see, e.g., [42,94,121]).

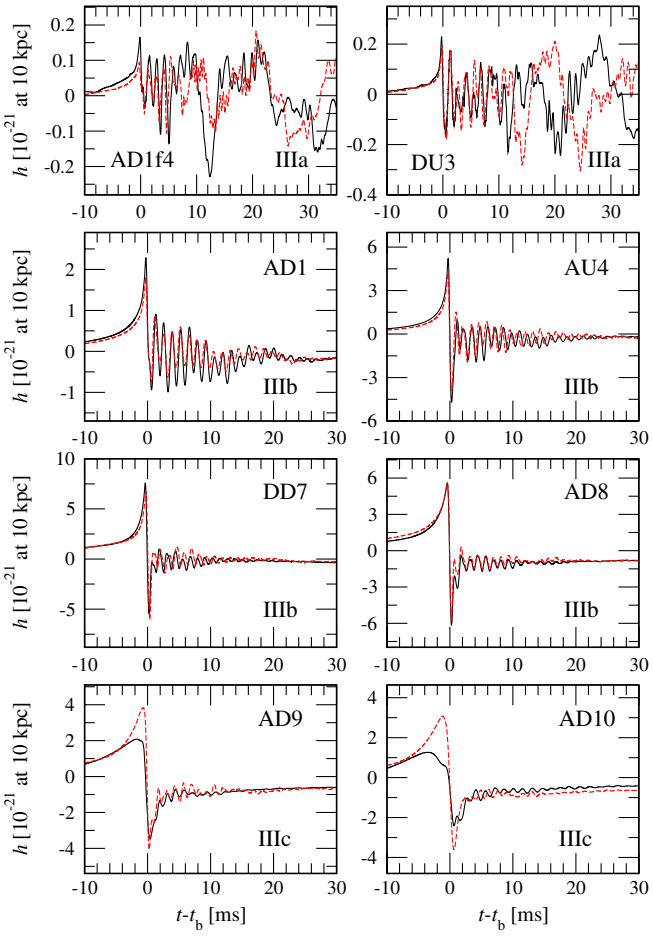

FIG. 15 (color online). Evolution of the dimensionless GW strain h (in units of 10^{-21} at a source distance of 10 kpc) as a function of postbounce time for representative models with different precollapse rotation profiles, central densities, and temperatures (low-T models with solid black lines and high-T with dashed red lines). Models with slow and (almost) uniform precollapse rotation (e.g., AD1f4 or DU3) develop considerable prompt postbounce convection visible as a dominating lower-frequency contribution in the waveform. Centrifugal effects damp this prompt convection and the waveforms of models with moderately rapid rotation (e.g., AD1, AU4, DD7, and AD8) and of rapidly rotating models (e.g., AD9 or AD10) exhibit no such contribution to the signal.

Type IIIb. In moderately rapidly rotating WDs that reach $0.7\% \lesssim \beta_{\rm ic,b} \lesssim 18\%$ and still experience a pressure-dominated bounce, convection is effectively suppressed due to a sufficiently large positive specific angular momentum gradient (e.g., [122]). Hence, there is no noticeable convective contribution to the postbounce GW signal (see, e.g., models AD1, AU4, DD7, AD8). For this signal subtype, the peak GW strain $|h|_{\rm max}$ is associated with the first positive peak, while relative values of the amplitudes of the first several peaks are similar to type IIIa.

Type IIIc. If rotation is sufficiently rapid and leading to $\beta_{\rm ic,b} \gtrsim 18\%$, the core bounces at subnuclear densities due to strong centrifugal support. This is reflected in the GW signal by an overall lower-frequency emission and a significant widening of the bounce peak of the waveform (see, e.g., models AD9, AD10). In some models of this subtype, the negative peak can be comparable to or slightly exceed that of the first positive peak in the waveform. This reflects the fact that the plunge acceleration is apparently reduced more significantly by rotation than is the reexpansion acceleration at core bounce. The postbounce ringdown peaks in all type IIIc models are smaller by a factor of $\gtrsim 2$ compared to the bounce signal. As pointed out in Sec. III B, uniformly rotating models do not rotate sufficiently rapidly to experience centrifugal bounce. Hence, they do not produce a type IIIc signal.

The AIC GW signal morphology is affected only slightly by variations in WD temperature and their resulting changes in the inner-core Y_e that are on the few-percent level for the range of precollapse temperatures considered here. In test calculations with more substantially increased inner-core values of Y_e (see Secs. II A 2 and II C 3) and, in turn, significantly larger values of $M_{\rm ic,b}$, we find signals that are intermediate between type III and type I.

Key quantitative results from our model simulations are summarized in Tables. II and IV. The waveform data for all models are available for download from [123].

A. Peak gravitational-wave amplitude

Across our entire model set, the peak GW amplitude $|h|_{\rm max}$ covers a range of almost 2 orders of magnitude, from $\sim 10^{-22}$ to $\sim 10^{-20}$ (at distance to the source of 10 kpc; see Table II). $|h|_{\rm max}$ depends on various parameters and it is difficult to provide a simple description of its systematics that encompasses all cases. In order to gain insight into how $|h|_{\rm max}$ depends on $\Omega_{\rm c,i}$, on differential rotation, on the initial $\rho_{\rm c}$, on the precollapse WD temperature, and on the degree of deleptonization in collapse, we describe below the effects of variations in one of these parameters while holding all others fixed.

(i) In a sequence of precollapse WDs with fixed differential rotation, $\rho_{\rm c}$, and T_0, the peak GW amplitude $|h|_{\rm max}$ increases steeply with $\Omega_{\rm c,i}$ in slowly rotating models that do not come close to being centrifugally supported. When centrifugal effects become dynamically important, $|h|_{\rm max}$ saturates at $\sim 7 \times 10^{-21}$ (at 10 kpc) and then decreases with increasing $\Omega_{\rm c,i}$. This reflects the fact that such rapidly spinning inner cores produced by AIC cannot reach high densities and high compactness and that the slowed-down collapse decreases the deceleration at bounce, thus reducing $|h|_{\rm max}$ and pushing the GW emission to lower frequencies.

(ii) In a sequence of precollapse WDs with fixed $\Omega_{\rm c,i}$, T_0, and $\rho_{\rm c}$, an increase in the degree of WD differential rotation leads to an increase in the amount of angular momentum present in the WD inner core at bounce. This translates into an increase of $|h|_{\rm max}$ in models that do not become centrifugally supported and experience a pressure-dominated bounce. The transition to centrifugal bounce is now reached at lower values of $\Omega_{\rm c,i}$ (see Sec. III B), so that the centrifugal saturation of $|h|_{\rm max}$ described above in (i) is reached at much smaller values of $\Omega_{\rm c,i}$.

(iii) In a sequence of precollapse WDs with fixed $\Omega_{\rm c,i}$, T_0, and differential rotation and varying $\rho_{\rm c}$, models with lower (higher) $\rho_{\rm c}$ yield larger (smaller) values of $|h|_{\rm max}$. This is because models that are initially less compact spin up more during collapse (cf. the discussion in Sec. III B). However, this systematics holds only as long as the model does not become centrifugally supported, which happens for lower (higher) $\rho_{\rm c}$ WDs at smaller (greater) $\Omega_{\rm c,i}$.

(iv) When only the WD temperature is varied, we find that for slowly to moderately rapidly rotating WDs, high-T models generally reach smaller $|h|_{\rm max}$ than their low-T counterparts. This is because high-T WDs yield smaller inner cores at bounce, which hold less angular momentum and, as a consequence, are less centrifugally deformed (see Table II and in Fig. 15). However, this behavior reverses in rapidly rotating WDs for which low-T models are more centrifugally affected and, hence, yield a smaller $|h|_{\rm max}$ than their high-T counterparts.

(v) If the degree of deleptonization is decreased by an *ad hoc* increase of inner-core Y_e (see Secs. II A 2 and II C 3) and all else is kept fixed, $M_{\rm ic,b}$ increases and for slowly to moderately rapidly rotating WDs, $|h|_{\rm max}$ increases. As for the low-T case discussed in the above, this behavior reverses in rapidly rotating WDs for which high-Y_e models are more centrifugally affected and yield smaller $|h|_{\rm max}$ than their lower-Y_e counterparts.

To demonstrate the dependence of $|h|_{\rm max}$ on the overall rotation of the inner core at bounce, we plot in Fig. 16 $|h|_{\rm max}$ as a function of the inner-core parameter $\beta_{\rm ic,b}$ at bounce for our high-T models. $|h|_{\rm max}$ depends primarily on $\beta_{\rm ic,b}$ and is rather independent of the particular precollapse configuration that leads to a given $\beta_{\rm ic,b}$. For small $\beta_{\rm ic,b}$ far away from the centrifugal limit, we find $|h|_{\rm max} \propto \beta_{\rm ic,b}^{0.74}$, where we have obtained the exponent by a power-law fit of high-T models with $1\% \lesssim \beta_{\rm ic,b} \lesssim 13\%$. This finding is in qualitative agreement with what [50] saw for iron core collapse. The overall maximum of $|h|_{\rm max}$ is reached in WDs that yield $\beta_{\rm ic,b} \sim 16\%$, beyond which $|h|_{\rm max}$ decreases with increasing $\beta_{\rm ic,b}$.

B. Gravitational-wave energy spectrum

The total energy emitted in GWs is in the range of $\sim 10^{-10} M_\odot c^2 \lesssim E_{\rm GW} \lesssim 2 \times 10^{-8} M_\odot c^2$ in the entire set

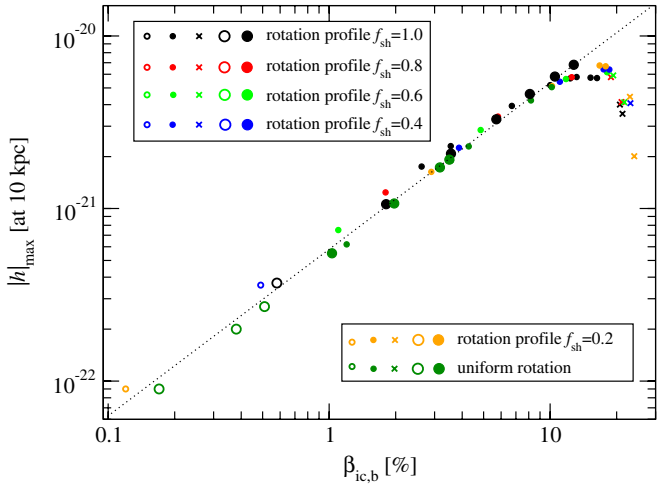

FIG. 16 (color online). Peak value $|h|_{max}$ of the GW amplitude at a source distance of 10 kpc distance for the burst signal of all models versus the parameter $\beta_{ic,b}$ of the inner core at the time of bounce. At slow to moderately rapid rotation, $|h|_{max}$ scales almost linearly with $\beta_{ic,b}$ (marked by the dotted straight line), while for $\beta_b \gtrsim 16\%$ centrifugal effects reduce $|h|_{max}$. The symbol convention for the various sets is explained in the caption of Fig. 8.

of models considered in this article. In Fig. 17, we plot the GW spectral energy density dE_{GW}/df of the three models AD1f3, AD4, and AD10 as representative examples of the three signal subtypes IIIa–IIIc. The top panel shows model AD1f3 as a representative pressure-dominated bounce model with prompt convection. In such models, there is a strong structured, but broad, contribution to the spectrum at low frequencies. The integral of such a contribution (which is present in all models with slow rotation) can exceed that from core bounce in these models. This is not the case in

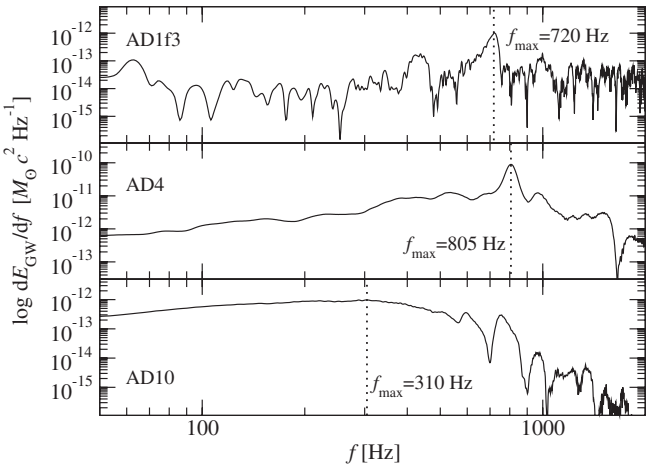

FIG. 17. Spectral energy density of the GW signal for representative AIC models AD1f3 (top panel), AD4 (center panel), and AD10 (bottom panel). f_{max} is the peak frequency of the GWs emitted at core bounce.

model AD1f3, whose GW burst from bounce is the one leading to the peak at $f_{max} = 720$ Hz.

The central panel of Fig. 17 depicts dE_{GW}/df of model AD4 as a representative pressure-dominated bounce model in which no significant postbounce convection occurs. The spectrum of this model exhibits a distinct and narrow high-frequency peak at $f_{max} \sim 805$ Hz. Finally, the bottom panel of Fig. 17 refers to model A10 that experiences centrifugal bounce. In this model, the dynamics is dominated by centrifugal effects, leading to low-frequency emission and $f_{max} = 310$ Hz, but higher-frequency components are still discernible and are most likely related to prolonged higher-frequency GW emission from the PNS ringdown.

In Fig. 18, we plot the peak frequencies f_{max} of the GW energy spectrum as a function of the inner-core parameter $\beta_{ic,b}$ for high-T AIC models (the low-T and higher-Y_e models show the same overall systematics). In models that undergo pressure-dominated bounce, f_{max} increases nearly linearly with $\beta_{ic,b}$ in the region $\beta_{ic,b} \lesssim 10\%$, while at $\beta_{ic,b}$ in the range of $10\% \lesssim \beta_{ic,b} \lesssim 20\%$, the growth of f_{max} saturates at ~800 Hz and f_{max} does not change significantly with further increase of rotation. For very rapid rotation ($\beta_{ic,b} \gtrsim 20\%$), f_{max} decreases steeply with $\beta_{ic,b}$, reaching a value of ~400 Hz at $\beta_{ic,b} \simeq 23\%$ (not shown in the figure, see Table IV).

While it is straightforward to understand the systematics of f_{max} at high $\beta_{ic,b}$ where centrifugal effects slow down collapse and thus naturally push the GW emission to low frequencies, the increase of f_{max} with rotation at low to intermediate $\beta_{ic,b}$ is less intuitive. If one assumes that the dominant GW emission at core bounce in all models is due to the quadrupole component of the fundamental quasiradial mode of the inner core, one would expect a monotonic decrease of f_{max} with increasing rotation and, hence, decreasing mean core density (see, e.g., [41]). A possible explanation for the increase of f_{max} at slow to moderately

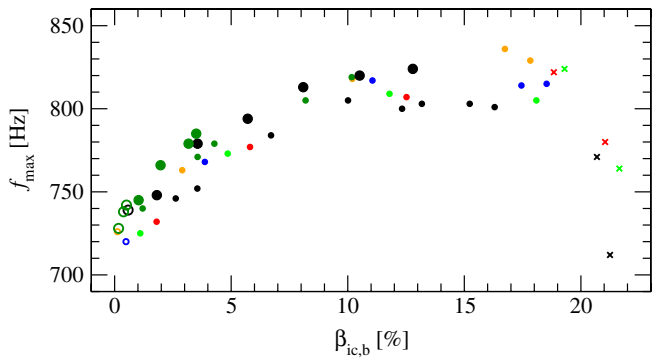

FIG. 18 (color online). Frequency f_{max} at the maximum of the GW spectral energy density in pressure-dominated bounce and a subset of centrifugal bounce models versus the parameter $\beta_{ic,b}$ of the inner core at bounce. The symbol convention for the various sets is explained in the caption of Fig. 8.

TABLE IV. GW signal characteristics for the high-T AIC models: $E_{\rm GW}$ is the total GW energy, $f_{\rm max}$ is the peak frequency of the GW energy spectrum, Δf_{50} is the frequency interval around $f_{\rm max}$ that emits 50% of $E_{\rm GW}$. The nonrotating models are omitted here.

AIC model	$E_{\rm GW}$ [$10^{-9} M_\odot c^2$]	$f_{\rm max}$ [Hz]	Δf_{50} [Hz]
AU1	1.1	742.7	31
AU2	5.7	782.7	28
AU3	7.8	786.7	27
AU4	15.7	816.0	49
AU5	17.0	831.9	120
DU1	0.1	768.0	343
DU2	0.3	770.0	556
DU3	0.4	747.0	473
DU4	0.9	745.0	304
DU5	2.0	765.7	26
DU6	4.6	778.3	21
DU7	5.8	788.3	20
AD1	2.2	752.6	33
AD2	3.7	765.4	30
AD3	8.7	790.5	37
AD4	11.8	812.5	115
AD5	14.2	813.6	173
AD6	15.0	815.0	201
AD7	15.5	815.1	220
AD8	13.8	811.0	245
AD9	1.8	806.0	413
AD10	1.0	304.0	126
DD1	0.3	740.0	324
DD2	1.4	746.7	62
DD3	4.6	780.1	21
DD4	9.3	793.6	22
DD5	15.2	813.7	21
DD6	18.5	820.2	48
DD7	22.3	826.9	152
AD1f1	1.3	745.7	54
AD1f2	0.6	731.4	69
AD1f3	0.2	726.5	315
AD1f4	0.1	737.0	476
AD3f1	7.7	787.0	36
AD3f2	7.0	781.2	31
AD3f3	5.5	777.2	27
AD3f4	3.7	769.8	27
AD6f1	15.7	818.0	175
AD6f2	16.0	819.5	165
AD6f3	16.0	822.6	145
AD6f4	15.8	827.6	123
AD9f1	5.4	805.5	323
AD9f2	11.8	813.0	273
AD9f3	15.9	833.0	263
AD9f4	19.5	844.0	254
AD10f1	1.9	808.0	137
AD10f2	5.8	809.0	333
AD10f3	12.1	826.6	269
AD10f4	16.5	840.0	263
AD11f2	3.4	794.0	105
AD12f3	0.8	165.5	44
AD12f4	1.4	231.0	73
AD13f4	0.07	62.5	60

rapid rotation is that the primary GW emission in these models is due to the fundamental quadrupole ^2f mode, whose frequency may increase with rotation. This has been demonstrated by Dimmelmeier, Stergioulas, and Font [124], who studied oscillation modes of sequences of $\gamma = 2$ polytropes. To confirm this interpretation, and following the technique of mode recycling outlined in [124], we perturb a subset of our postbounce cores with the eigenfunction of the ^2f mode of a Newtonian nonrotating neutron star. As expected, we find that the resulting dynamics of the postbounce core is dominated by a single oscillation mode with a frequency that matches within $\lesssim 10\%$ the peak frequency $f_{\rm max}$ of $dE_{\rm GW}/df$ of the corresponding slowly or moderately rapidly rotating AIC model. The interesting details of the mode structure of the inner cores of AIC and iron core collapse will receive further scrutiny in a subsequent publication.

Finally, in Fig. 19, we provide time-frequency analyses of the GW signals of the same representative models shown in Fig. 17. The analysis is carried out with a short-time Fourier transform employing a Gaussian window with a width of 2 ms and a sampling interval of 0.2 ms. In all three cases, the core bounce is clearly visible and marked by a broadband increase of the emitted energy. The slowly rotating model AD1f3 emits its strongest burst at 600–800 Hz ($f_{\rm max} = 720$ Hz) and subsequently exhibits broadband emission with significant power at lower frequencies due to prompt convection. Model AD4 is more rapidly rotating and shows significant prebounce low-frequency emission due to its increased rotational deformation. At bounce, a strong burst, again with power at all frequencies, but primarily at frequencies about its $f_{\rm max} = 805$ Hz, is emitted. Much of the postbounce $E_{\rm GW}$ is emitted through ringdown oscillations at $f_{\rm max}$ that may be related to the ^2f mode of this model's PNS. Finally, in the rapidly rotating and centrifugally bouncing model AD10, we observe again low-frequency emission before bounce, but only a small increase of the primary emission band at bounce to $\sim$200–400 Hz. Nevertheless, there is still an appreciable energy emitted from higher-frequency components of the dynamics at bounce and postbounce times.

C. Comparing GW signals from AIC and iron core collapse

Recent studies [50,63,64,79] have shown that the collapse of rotating iron cores (ICC) produces GW signals of uniform morphology (so-called type I signals, see, e.g., [76]) that generically show one pronounced spike associated with core bounce with a subsequent ringdown and are similar to the type III signals found here for AIC. As in the AIC case, the GW signal of ICC has subtypes for slow, moderately rapid, and very rapid rotation. For comparing AIC and ICC GW signals, we chose three representative AIC models and then picked three ICC models with similar $\beta_{\rm ic,b}$ from the study of Dimmelmeier *et al.* [50], whose

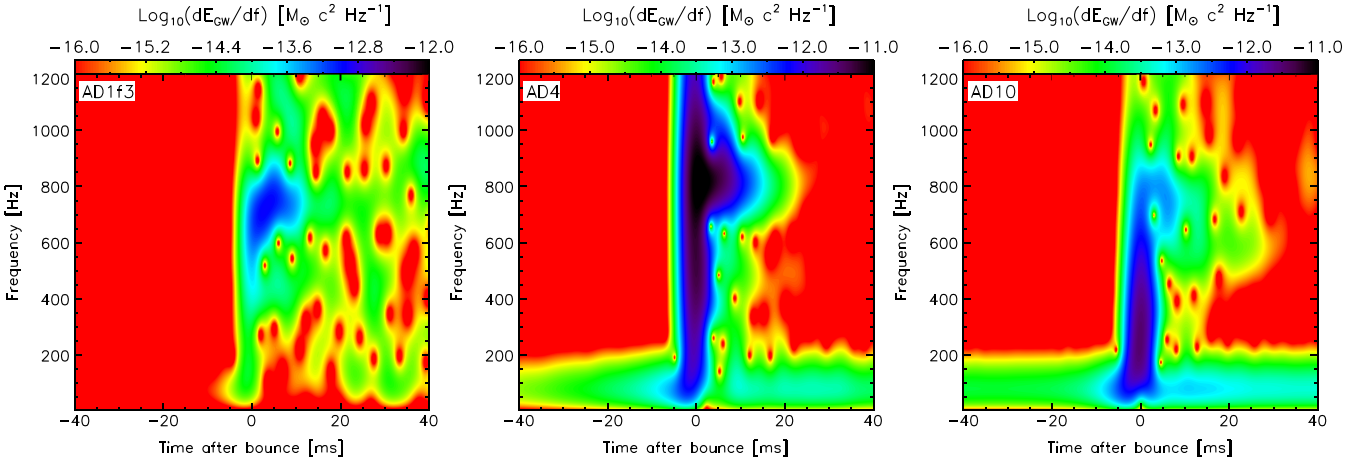

FIG. 19 (color online). Time-frequency color maps of the GW signals of models AD1f3 (type IIIa), AD4 (type IIIb), and AD10 (type IIIc, see also Fig. 17). Plotted is the "instantaneous" spectral GW energy density $dE_{\rm GW}/df$ in a 2 ms Gaussian window as a function of postbounce time. Note the prebounce low-frequency contribution in the moderately rapidly rotating models (model AD4, center panel) and rapidly rotating models (model AD10, right panel). The range of the colormap of the left panel (model AD1f3) is smaller by one dex than those of the other panels.

waveforms are freely available from [125]. This should ensure that we compare collapse models that are similarly affected by centrifugal effects for a one-to-one comparison. However, one should keep in mind that the inner-core masses $M_{\rm ic,b}$ at bounce of ICC models are generally larger by $\sim$0.2–0.3$M_\odot$ than in our AIC models (see Sec. III A).

In Fig. 20 we present this comparison and plot the GW signals of the high-T AIC models DU2 (slow rotation, type IIIa), AU5 (moderately rapid rotation, type IIIb), and AD10 (very rapid rotation, type IIIc). In the same order, we superpose the GW signals of the Dimmelmeier *et al.* [50] models s20A1O05, s20A3O07, and s20A3O15. These models started with the precollapse iron core of a $20M_\odot$ star and were run with the same code, EOS, and deleptonization algorithm as our AIC models, though with different, ICC specific $Y_e(\rho)$ trajectories.

The left panel of Fig. 20 compares the slowly rotating models DU2 and s20A1O05 that undergo pressure-dominated bounce and exhibit strong postbounce convection. As pointed out before, the latter is most likely overestimated in our current approach as well as in Dimmelmeier *et al.*'s. Note that the width of the waveform peaks associated with core bounce is very similar, indicating very similar emission frequencies. Model s20A1O05 exhibits a significantly larger signal amplitude at bounce. This is due to s20A1O05's larger $M_{\rm ic,b}$ but also to the fact that its $\beta_{\rm ic,b}$ is $\sim$0.7% compared to the $\sim$0.4% of DU2 (a closer match was not available from [125]). The prompt convection in model s20A1O05 is more vigorous and generates a larger-amplitude GW signal than in model DU2. This is due to the much steeper density gradient in the WD core that allows the AIC shock to remain stronger

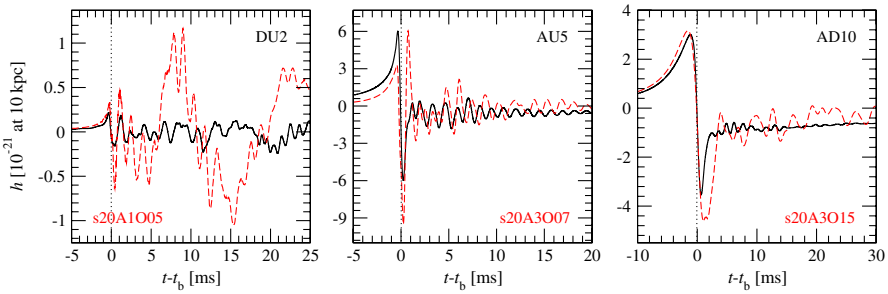

FIG. 20 (color online). Evolution of GW signals in the high-T AIC models DU2, AU5, AD10 (black solid lines) and three massive star iron-core-collapse models s20A1O05, s20A3O07, and s20A3O15 (red dashed lines) from the model set of Dimmelmeier *et al.* [50]. The AIC model DU2 and the iron-core-collapse model s20A1O05 undergo pressure-dominated bounce with significant prompt convection. Models AU5 and s20A3O7 experience pressure-dominated bounce without significant convection, and models AD10 and s20A3O15 undergo centrifugal bounce. The inner cores of models DU2, AU5, and AD10 (s20A1O05, s20A3O07, and s20A3O15) reach values of $\beta_{\rm ic,b}$ of about 0.4%, 10.2%, and 21.3% (0.7%, 10.1%, and 21.6%). Times are given relative to the time of core bounce which we mark with a vertical line.

out to larger radii. Hence, it leaves behind a shallower negative entropy gradient, leading to weaker convection and postbounce GW emission.

In the central panel of Fig. 20 we compare two moderately rapidly rotating models with nearly identical $\beta_{\rm ic}$ of $\sim$10%. Both models show a prebounce rise due to the inner core's accelerated collapse in the plunge phase. The AIC inner core, owing to its lower Y_e and weaker pressure support, experiences greater acceleration and emits a higher-amplitude signal than its ICC counterpart in this phase. At bounce, the stiff nuclear EOS decelerates the inner core, leading to the large negative peak in the GW signal. Because of the more massive inner core in ICC and since the EOS governing the dynamics is identical in both models, the magnitude of this peak is greater in the ICC model. Following bounce, the ICC model's GW signal exhibits a large positive peak of comparable or larger amplitude than the prebounce maximum. This peak is due to the recontraction of the ICC inner core after the first strong expansion after bounce. With increasing rotation, this recontraction and the associated feature in the waveform become less pronounced. On the other hand, due to its smaller inertia, the AIC inner core does not significantly overshoot its new postbounce equilibrium during the postbounce expansion. Hence, there is no appreciable postbounce recontraction and no such large positive postbounce peak in the waveform.

Example waveforms of AIC and ICC models experiencing core bounce governed by centrifugal forces are shown in the right panel of Fig. 20. In this case, the prebounce plunge dynamics are significantly slowed down by centrifugal effects, and the GW signal evolution is nearly identical in AIC and ICC. At bounce, the more massive inner core of the ICC model leads to a larger and broader negative peak in the waveform, and its ringdown signal exhibits larger amplitudes than in its AIC counterpart.

Finally, we consider AIC models with variations in the inner-core Y_e due to either different precollapse WD temperatures or *ad hoc* changes of the $\bar{Y}_e(\rho)$ parametrization (see Secs. II A 2 and II C 3). Lower-T WDs yield larger inner-core values of Y_e and, in turn, larger $M_{\rm ic,b}$ and GW signals that are closer to their iron-core counterparts. The same is true for models in which we impose an increased inner-core Y_e: AIC models with inner-core Y_e 10% larger than predicted by [28] still show clear type III signal morphology, while models with 20% larger Y_e fall in between type III and type I.

To summarize this comparison: Rotating AIC and rotating ICC lead to qualitatively and quantitatively fairly similar GW signals that most likely could not be distinguished by only considering general signal characteristics, such as maximum amplitudes, characteristic frequencies, and durations. A detailed knowledge of the actual waveform would be necessary, but even in this case, a distinction between AIC and ICC on the basis of the comparison presented here would be difficult. It could only be made for moderately rapidly spinning cores based on the presence (ICC, type Ib) or absence (AIC, type IIIb) of a first large positive peak in the waveform, but, again, only if AIC inner cores indeed have significantly smaller Y_e than their iron-core counterparts. ICC and AIC waveforms of types Ia/IIIa and Ic/IIIc are very similar. Additional astrophysical information concerning the distance to the source and its orientation as well as knowledge of the neutrino and electromagnetic signatures will most likely be necessary to distinguish between AIC and ICC.

D. Detection prospects for the gravitational-wave signal from AIC

In order to assess the detection prospects for the GW signal from AIC, we evaluate the characteristic signal frequency $f_{\rm c}$ and the dimensionless characteristic GW amplitude $h_{\rm c}$. Both quantities are detector dependent and are computed using Eqs. (14) and (15), respectively.

In Fig. 21, we show $h_{\rm c}$ for all models as a function of $f_{\rm c}$ for an initial 4 km Laser Interferometer Gravitational Wave Observatory (LIGO) detector, assuming a source distance of 10 kpc. For comparison with detector sensitivity, we include initial LIGO's design $h_{\rm rms}$ curve [126]. The distribution of our set of models in this figure obeys simple systematics. A number of very slowly rotating models that undergo pressure-dominated bounce with prompt convection (type IIIa) form a cluster in frequency in one region (near arrow 1). These models have the overall lowest values of $h_{\rm c}$ and exhibit low values of $f_{\rm c}$ in the range of 130–350 Hz. Both $f_{\rm c}$ and $h_{\rm c}$ grow with increasing rotation (along arrow 1). For the pressure-dominated bounce models without significant prompt convection (type IIIb), $h_{\rm c}$ grows with increasing rotation (along arrow 2), now at

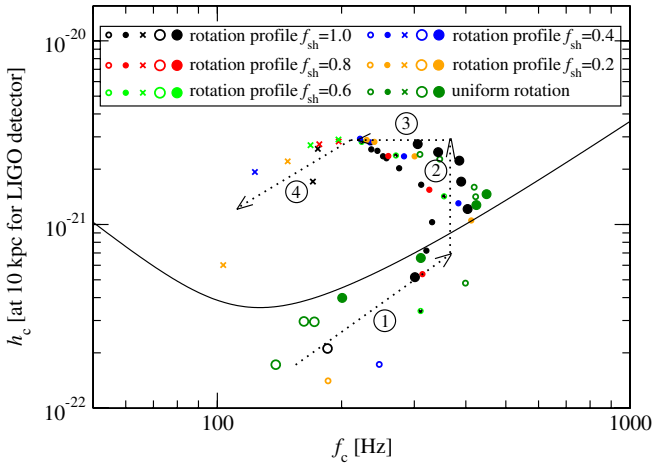

FIG. 21 (color online). Detector-dependent characteristic amplitudes of the GW signals of all models at an assumed distance of 10 kpc. The symbol convention for the various sets is described in the caption of Fig. 8. See the text for a discussion of the numbers and arrows.

practically constant f_c of ~350 Hz. Even for these models, f_c is always lower than the typical peak frequency f_{max} ~ 700–800 Hz of their spectral GW energy densities. This is due to the specific characteristics of the LIGO detector, whose highest sensitivity is around 100 Hz, thus leading to a systematic decrease of f_c with respect to f_{max}.

In more rapidly rotating models, centrifugal effects become more important, leading to greater rotational deformation of the inner core, but also slowing down the dynamics around core bounce, ultimately limiting h_c and reducing f_c (along arrow 3). Models that rotate so rapidly that they undergo centrifugal bounce (type IIIc) cluster in a separate region in the $h_c - f_c$ plane (along arrow 4), somewhat below the maximum value of h_c and at considerably lower f_c. The systematics for the lower-T models and for other detectors is very similar. Not surprisingly, given the analogies in the two signals, a similar behavior of h_c and f_c was observed in the context of rotating iron core collapse [50].

Figure 22 provides the same type of information shown in Fig. 21 but also for the advanced LIGO detector when the source is at 0.8 kpc (e.g., within the Andromeda galaxy), or for the proposed Einstein telescope (ET) [127] and a source distance of 5 Mpc. Initial LIGO is sensitive only to GWs coming from a moderately rapidly or rapidly rotating AIC event in the Milky Way, but its advanced version will probably be able to reveal sources also outside the Galaxy, although only within the local group. Finally, third-generation detectors such as ET, may be sensitive enough to detect some AIC events out to ~5 Mpc.

As pointed out in Secs. IV A and IV B, the GW signal amplitudes and the spectral GW energy distribution is

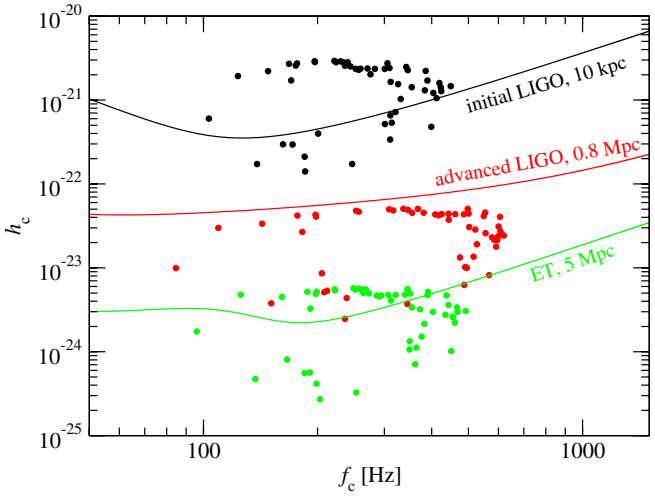

FIG. 22 (color online). Location of the GW signals from core bounce in the $h_c - f_c$ plane relative to the sensitivity curves of various interferometer detectors (as color-coded) for an extended set of models AD. The sources are at a distance of 10 kpc for LIGO, 0.8 Mpc for advanced LIGO, and 5 Mpc for the Einstein telescope.

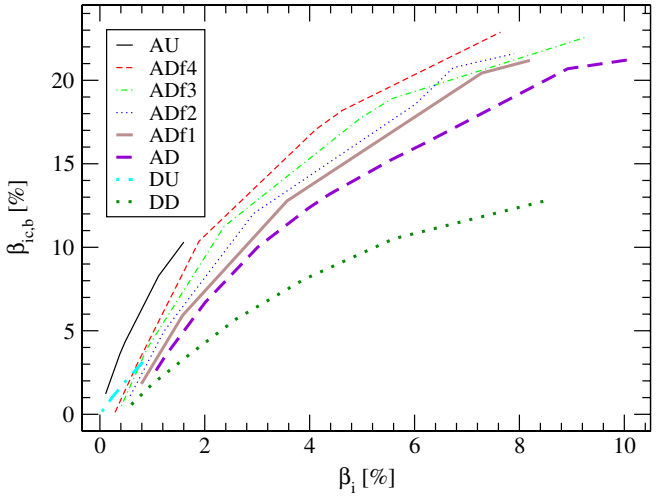

FIG. 23 (color online). The inner-core parameter $\beta_{ic,b}$ at bounce is plotted as a function of the precollapse parameter β_i for high-T models. Because of different central densities and rotation profiles of the precollapse WD models, there is no one-to-one correspondence between $\beta_{ic,b}$ and β_i. Hence, although one can extract $\beta_{ic,b}$ accurately from the bounce AIC GW signal, it is impossible to put strong constraints on β_i using the GW signal.

determined primarily by $\beta_{ic,b}$. Hence, given the systematics shown in Fig. 21, one may be optimistic about being able to infer $\beta_{ic,b}$ to good precision from the observation of GWs from a rotating AIC event. For example, as demonstrated in Fig. 18, even the knowledge of only f_{max} can put some constraints on $\beta_{ic,b}$. However, inferring accurately the properties of the progenitor WD using exclusively information provided by GWs may be extremely difficult given the highly degenerate dependence of $\beta_{ic,b}$ on the various precollapse WD model parameters discussed in Sec. III B. To elaborate on this point, we show in Fig. 23 the relation between $\beta_{ic,b}$ and the precollapse WD parameter β_i. Even if GWs can provide good constraints on $\beta_{ic,b}$, a rather large variety of models with different initial rotational properties would be able to lead to that same $\beta_{ic,b}$, and additional astrophysical information on the progenitor will be needed to determine the precollapse rotational configuration. The only exception to this is the possibility of ruling out uniform WD progenitor rotation if $\beta_{ic,b} \gtrsim 18\%$ (cf. Sec. III B).

V. PROSPECTS FOR NONAXISYMMETRIC ROTATIONAL INSTABILITIES

Nonaxisymmetric rotational instabilities in PNSs formed in AIC or iron core collapse have long been proposed as strong and possibly long-lasting sources of GWs (see, e.g., [42] for a recent review). The postbounce GW emission by nonaxisymmetric deformations of rapidly rotating PNSs could be of similar amplitude as the signal

from core bounce and, due to its potentially much longer duration, could exceed it in emitted energy (e.g., [63–65]). Moreover, since the characteristic GW amplitude h_c scales with the square root of the number of cycles, the persistence of the nonaxisymmetric dynamics for many rotation periods can drastically increase the chances for detection.

The simulations presented in this paper impose axisymmetry; hence we are unable to track the formation and evolution of rotationally induced nonaxisymmetric structures. Nonetheless, since the dynamical high-β instability can develop only at β above $\beta_{\rm dyn} \simeq 0.25$ [55,56], we can still assess the prospects for such instabilities by studying the values of β reached by our AIC models. Moreover, as we shall see below, the analysis of the rotational configuration of the newly formed PNS can give a rough idea about the outlook also for low-β instabilities.

As shown in Sec. III B, for not very rapidly rotating models, the parameter $\beta_{\rm ic,b}$ of the inner core at bounce increases with the progenitor rotation and saturates at $\sim$24.5% (see Fig. 10). Immediately after bounce, the inner core reexpands and, after undergoing several damped oscillations, settles into a new quasiequilibrium state with a $\beta_{\rm ic,pb}$ typically smaller by $\sim$3% (in relative value) than that at bounce. The highest value of $\beta_{\rm ic,pb}$ of our entire model set is $\sim$24% (observed in model AD12f4) and most other rapidly rotating models reach values of $\beta_{\rm ic,pb}$ that are well below this value (cf. Table II). Hence, we do not expect the high-β instability to occur immediately after bounce in most AIC events.

On the other hand, the matter around the PNS experiences rapid neutrino cooling (not modeled by our approach) and the PNS contracts significantly already in the early postbounce phase. This results in spin-up and in a substantial increase of $\beta_{\rm ic,pb}$. Using the VULCAN/2D code, Ott [61] studied the postbounce evolution of the PNS rotation of the Dessart *et al.* AIC models [28]. He found that, in the case of the rapidly rotating $1.92M_\odot$ model, the postbounce contraction leads to a growth of $\beta_{\rm ic,pb}$ by $\sim$50% from $\sim$14% to $\sim$22% in the initial $\sim$50 ms after bounce. We expect that a similar increase of the parameter $\beta_{\rm ic,pb}$ should take place also for the rapidly rotating AIC models considered here. More specifically, if we assume that β increases by $\sim$50% within $\sim$50 ms after bounce, we surmise that AIC models with $\beta_{\rm ic,b} \gtrsim 17\%$ at bounce should reach $\beta_{\rm ic,pb} \gtrsim \beta_{\rm dyn}$ within this postbounce interval and thus become subject to the high-β dynamical instability.

As mentioned in Sec. III B, uniformly rotating WDs cannot reach $\beta_{\rm ic,pb}$ in excess of $\sim$10.5%. Hence, they are unlikely to become subject to the high-β dynamical nonaxisymmetric instability, but may contract and spin up to $\beta \geq \beta_{\rm sec} \simeq 14\%$ at which they, in principle, could experience a secular nonaxisymmetric instability in the late postbounce phase. However, other processes, e.g., MHD dynamos and instabilities (see, e.g., [128,129]), may limit and/or decrease the PNS spin on the long time scale needed by a secular instability to grow.

In addition to the prospects for the high-β instability, the situation appears favorable for the low-β instability as well. The latter can occur at much lower values of β as long as the PNS has significant differential rotation (see, e.g., [58,59,62,64–67] and references therein). While this instability's true nature is not yet understood, a necessary condition for its development seems to be the existence of a corotation point inside the star, i.e., a point where the mode pattern speed coincides with the local angular velocity [66,130]. Bearing in mind that the lowest-order unstable modes have pattern speeds of the order of the characteristic Keplerian angular velocity $\mathcal{O}(\Omega_{\rm char})$ [57], we can easily verify whether such a criterion is ever satisfied in our models. Assuming a characteristic mass of the early postbounce PNS of $\sim 0.8M_\odot$ and a radius of $\sim$20 km, we obtain a characteristic Keplerian angular velocity of $\Omega_{\rm char} \sim 4\ {\rm rad\,m\,s^{-1}}$. Because most AIC models that reach $\beta_{\rm ic,pb} \gtrsim 15\%$ have a peak value of $\Omega \gtrsim 5\ {\rm rad\,ms^{-1}}$, it is straightforward to conclude that these models will have a corotation point and, hence, that the low-β instability may be a generic feature of rapidly rotating AIC. We note that even uniformly rotating precollapse models have strong differential rotation in the postshock region outside the inner core. However, further investigation is needed to infer whether such models may be also be subject to low-β dynamical instability.

As a concluding remark we stress that the above discussion is based on simple order-of-magnitude estimates and is therefore rather inaccurate. Reliable estimates can be made only by performing numerical simulations in 3D that adequately treat the postbounce deleptonization and contraction of the PNS and that investigate the dependence of the instability on $\beta_{\rm ic,pb}$, on the degree of differential rotation, and on the thermodynamic and MHD properties of the PNS. Finally, these calculations will also establish what is the effective long-term dynamics of the bar-mode deformation. In simulations of isolated polytropes [55,56] and from perturbative calculations [131], it was found that coupling among different modes tends to counteract the bar-mode instability on a dynamical time scale after its development. It is yet unclear whether this behavior will be preserved also in the AIC scenario, where infalling material with high specific angular momentum may lead to significant changes. This will be the subject of future investigations.

VI. SUMMARY AND CONCLUSIONS

In this paper we have presented the first general-relativistic simulations of the axisymmetric AIC of massive white dwarfs to protoneutron stars. Using the general-relativistic hydrodynamics code COCONUT, we performed 114 baseline model calculations, each starting from a 2D equilibrium configuration, using a finite-temperature mi-

crophysical EOS, and a simple, yet effective, parametrization scheme of the electron fraction Y_e that provides an approximate description of deleptonization valid in the collapse, bounce, and very early postbounce phases. The precollapse structure and rotational configuration of WDs that experience AIC is essentially unconstrained. This prompted us to carry out this work. With our large set of model calculations, we have investigated the effects on the AIC evolution of variations in precollapse central density, temperature, central angular velocity, differential rotation, and deleptonization in collapse. The inclusion of general relativity enabled us to correctly describe the AIC dynamics, and our extended model set allowed us for the first time to study systematically GW emission in the AIC context.

We find that the overall dynamics in the collapse phase of AIC events is similar to what has long been established for rotating iron core collapse. A universal division in homologously collapsing inner core and supersonically infalling outer core obtains and the self-similarity of the collapse nearly completely washes out any precollapse differences in stellar structure in the limit of slow rotation. Because of the high degeneracy of the electrons in the cores of AIC progenitor WDs, electron capture is predicted to be strong already in early phases of collapse [28], leading to a low trapped lepton fraction and consequently small inner-core masses $M_{\rm ic,b}$ at bounce of around $0.3M_\odot$ which decrease somewhat with increasing precollapse WD temperature due to the temperature-dependent abundance of free protons. Test calculations motivated by potential systematic biases of the AIC $\bar{Y}_e(\rho)$ trajectories obtained from [28] (see Secs. II A 2 and II C 3) with inner-core values of Y_e increased by $\sim$10%, and $\sim$20% yielded values $M_{\rm ic,b}$ larger by $\sim$11% and $\sim$25%.

Our simulations show that rotation can have a profound influence on the AIC dynamics, but will always stay subdominant in the collapse of uniformly rotating WDs whose initial angular velocity is constrained by the Keplerian limit of surface rotation. In rapidly differentially rotating WDs, on the other hand, centrifugal support can dominate the plunge phase of AIC and lead to core bounce at subnuclear densities. We find that the parameter $\beta_{\rm ic,b} = (E_{\rm rot}/|W|)_{\rm ic,b}$ of the inner core at bounce provides a unique mapping between inner-core rotation and late-time collapse and bounce dynamics, but the mapping between precollapse configurations and $\beta_{\rm ic,b}$ is highly degenerate, i.e., multiple; in many cases very different precollapse configurations of varying initial compactness and total angular momentum can yield practically identical $\beta_{\rm ic,b}$ and corresponding collapse/bounce dynamics.

Recent phenomenological work presented in [30,49] on the potential EM display of an AIC event has argued for both uniform WD rotation [49,102] and massive quasi-Keplerian accretion disks left behind at low latitudes after AIC shock passage. The analysis of our extensive model set, on the other hand, shows that uniformly rotating WDs produce no disks at all or, in extreme cases that are near mass shedding at the precollapse stage, only very small disks ($M_{\rm disk} \lesssim 0.03M_\odot$). Only rapidly differentially rotating WDs yield the large disk masses needed to produce the enhanced EM signature proposed in [30,49].

An important focus of this work has been on the GW signature of AIC. GWs, due to their inherently multidimensional nature, are ideal messengers for the rotational dynamics of AIC. We find that all AIC models following our standard $\bar{Y}_e(\rho)$ parametrizations yield GW signals of a generic morphology which has been classified previously as type III [61,76,78]. This signal type is due primarily to the small inner-core masses at bounce obtained in these models. We distinguish between three subtypes of AIC GW signals. Type IIIa occurs for $\beta_{\rm ic,b} \lesssim 0.7\%$ (slow rotation), is due in part to early postbounce prompt convection, and results in peak GW amplitudes $|h_{\rm max}| \lesssim 5 \times 10^{-22}$ (at 10 kpc) and emitted energies $E_{\rm GW} \lesssim$ few $\times 10^{-9} M_\odot c^2$. Most of our AIC models produce type IIIb GW signals that occur for $0.7\% \lesssim \beta_{\rm ic,b} \lesssim 18\%$ (moderate/moderately rapid rotation) and yield $6 \times 10^{-22} \lesssim |h_{\rm max}|(\text{at } 10\,\text{kpc}) \lesssim 8 \times 10^{-21}$ and emitted energies of $9 \times 10^{-10} M_\odot c^2 \lesssim E_{\rm GW} \lesssim 2 \times 10^{-8} M_\odot c^2$. Rotation remains subdominant in type IIIa and type IIIb models and we find that there is a monotonic and near-linear relationship between maximum GW amplitude and the rotation of the inner core which is best described by the power law $|h_{\rm max}| \propto 10^{-21} \beta_{\rm ic,b}^{0.74}$. Furthermore, we find that the frequencies $f_{\rm max}$ at which the GW spectral energy densities of type IIIa and IIIb models peak are in a rather narrow range from $\sim$720 Hz to $\sim$840 Hz and exhibit a monotonic growth from the lower to the upper end of this range with increasing rotation. This finding suggests that the GW emission in these models is driven by the fundamental quadrupole (^2f) mode of the inner core.

In the dynamics of AIC models that reach $\beta_{\rm ic,b} \gtrsim 18\%$, centrifugal effects become dominant and lead to core bounce at subnuclear densities. Such models must be differentially rotating at the onset of collapse and produce type IIIc GW signals with maximum amplitudes of $4.0 \times 10^{-22} \lesssim |h_{\rm max}|(\text{at } 10\,\text{kpc}) \lesssim 5.5 \times 10^{-21}$, emitted energies of $10^{-10} M_\odot c^2 \lesssim E_{\rm GW} \lesssim 10^{-8} M_\odot c^2$, and peak frequencies of $62\,\text{Hz} \lesssim f_{\rm max} \lesssim 800\,\text{Hz}$. In contrast to type IIIa and IIIb models, in type IIIc models, $|h_{\rm max}|$, $E_{\rm GW}$, and $f_{\rm max}$ decrease monotonically with increasing $\beta_{\rm ic,b}$.

Combining the information from signal morphology, $|h_{\rm max}|$, $E_{\rm GW}$, and $f_{\rm max}$, we conclude that already first-generation interferometer GW detectors should be able to infer the rotation of the inner core at bounce (as measured by $\beta_{\rm ic,b}$) from a Galactic AIC event. Because of the degenerate dependence of $\beta_{\rm ic,b}$ on initial model parameters, this can put only loose constraints on the structure and rotational configuration of the progenitor WD. However, the observation of an AIC with $\beta_{\rm ic,b} \gtrsim 18\%$ would rule out uniform progenitor rotation.

Studying the configurations of the protoneutron stars formed in our AIC models, we find that none of them are likely to experience the high-β nonaxisymmetric bar-mode instability at very early postbounce times. We estimate, however, that all models that reach $\beta_{\mathrm{ic,b}} \gtrsim 17\%$ will contract and reach the instability threshold within $\sim$50 ms after bounce. Less rapidly spinning models will require more time or will go unstable to the low-β instability. The latter requires strong differential rotation which is ubiquitous in the outer PNS and in the postshock region of our AIC models. AIC progenitors, due to their evolution through accretion or formation through merger, are predestined to be rapidly rotating and form PNSs that are likely to become subject to nonaxisymmetric instabilities. This is in contrast to the precollapse iron cores of ordinary massive stars that are expected to be mostly slowly spinning objects [51,53]. We conclude that the appearance of nonaxisymmetric dynamics driven by either the low-β or high-β instability and the resulting great enhancement of the GW signature may be a generic aspect of AIC and must be investigated in 3D models.

The comparison of the GW signals of our axisymmetric AIC models with the gravitational waveforms of the iron-core-collapse models of Dimmelmeier *et al.* [50] reveals that the overall characteristics of the signals are rather similar. It appears unlikely that AIC and iron core collapse could be distinguished on the basis of the axisymmetric parts of their GW signals alone, unless detailed knowledge of the signal time series as well as of source orientation and distance is available to break observational degeneracies.

The results of our AIC simulations presented in this paper and the conclusions that we have drawn on their basis demonstrate the complex and in many cases degenerate dependence of AIC outcomes and observational signatures on initial conditions. The observation of GWs from an AIC event can provide important information on the rotational dynamics of AIC. However, to lift degeneracies in model parameters and gain full insight, GW observations must be complemented by observations of neutrinos and electromagnetic waves. These multimessenger observations require underpinning by comprehensive and robust computational models that have no symmetry constraints and include all the necessary physics to predict neutrino, electromagnetic, and GW signatures.

As a point of caution, we note that the generic type III GW signal morphology observed in our AIC models is due to the small inner-core values of Y_e and consequently small inner-core masses predicted by the $\bar{Y}_e(\rho)$ parametrization obtained from the approximate Newtonian radiation-hydrodynamic simulations of [28]. Tests with artificially reduced deleptonization show that the signal shape becomes a mixture of type III found in our study and type I observed in rotating iron core collapse [50] if the Y_e in the inner core is larger by $\sim$20%. In a follow-up study, we will employ $\bar{Y}_e(\rho)$ data from improved general-relativistic radiation-hydrodynamics simulations [103] to better constrain the present uncertainties of the AIC inner-core electron fraction.

Although performed using general-relativistic hydrodynamics, the calculations discussed here are limited to conformally flat spacetimes and axisymmetry. We ignored postbounce deleptonization, neutrino cooling, and neutrino heating. We also neglected nuclear burning, employed only a single finite-temperature nuclear EOS, and were forced to impose *ad hoc* initial temperature and electron fraction distributions onto our precollapse WD models in rotational equilibrium. Future studies must overcome the remaining limitations to build accurate models of AIC. Importantly, extensive future 3D radiation-hydrodynamic simulations are needed to address the range of possible, in many cases probably nonaxisymmetric, postbounce evolutions of AIC and to make detailed predictions of their signatures in GWs, neutrinos, and the electromagnetic spectrum.

ACKNOWLEDGMENTS

It is a pleasure to thank Alessandro Bressan, Adam Burrows, Frank Löffler, John Miller, Stephan Rosswog, Nikolaos Stergioulas, Sung-Chul Yoon, Shin Yoshida, and Burkhard Zink for helpful comments and discussions. This work was supported by the Deutsche Forschungsgemeinschaft through the Transregional Collaborative Research Centers SFB/TR 27 "Neutrinos and Beyond," SFB/TR 7 "Gravitational Wave Astronomy," by the Cluster of Excellence EXC 153 "Origin and Structure of the Universe" (http://www.universe-cluster.de), and by "CompStar," a Research Networking Programme of the European Science Foundation. C. D. O. acknowledges partial support by the National Science Foundation under Grant No. AST-0855535. The simulations were performed on the computer clusters of the Albert Einstein Institute, on machines of the Louisiana Optical Network Initiative under allocation LONI_numrel04, and on the NSF Teragrid under allocation TG-MCA02N014.

[1] F. Herwig, Annu. Rev. Astron. Astrophys. **43**, 435 (2005).
[2] S. E. Woosley, A. Heger, and T. A. Weaver, Rev. Mod. Phys. **74**, 1015 (2002).
[3] A. J. T. Poelarends, F. Herwig, N. Langer, and A. Heger, Astrophys. J. **675**, 614 (2008).
[4] S. Chandrasekhar, *Stellar Structure* (Dover, New York,

USA, 1938).
[5] L. S. Shapiro and S. A. Teukolsky, *Black Holes, White Dwarfs and Neutron Stars* (John Wiley and Sons, New York, USA, 1983).
[6] J. P. Ostriker and P. Bodenheimer, Astrophys. J. **151**, 1089 (1968).
[7] S.-C. Yoon and N. Langer, Astron. Astrophys. **419**, 623 (2004).
[8] H. A. Bethe, Rev. Mod. Phys. **62**, 801 (1990).
[9] K. Nomoto, Astrophys. J. **277**, 791 (1984).
[10] J. Gutiérrez, R. Canal, and E. García-Berro, Astron. Astrophys. **435**, 231 (2005).
[11] M. Livio, in *Type Ia Supernovae, Theory and Cosmology*, edited by J. C. Niemeyer and J. W. Truran (Cambridge University Press, Cambridge, England, 2000), p. 33.
[12] L. Siess, Astron. Astrophys. **448**, 717 (2006).
[13] I. J. Iben, C. Ritossa, and E. Garcia-Berro, Astrophys. J. **489**, 772 (1997).
[14] C. Ritossa, E. Garcia-Berro, and I. J. Iben, Astrophys. J. **460**, 489 (1996).
[15] R. Canal and E. Schatzman, Astron. Astrophys. **46**, 229 (1976).
[16] H. Saio and K. Nomoto, Astron. Astrophys. **150**, L21 (1985).
[17] K. Nomoto, Prog. Part. Nucl. Phys. **17**, 249 (1986).
[18] R. Mochkovitch and M. Livio, Astron. Astrophys. **209**, 111 (1989).
[19] K. Nomoto and Y. Kondo, Astrophys. J. Lett. **367**, L19 (1991).
[20] H. Saio and K. Nomoto, Astrophys. J. **500**, 388 (1998).
[21] T. Uenishi, K. Nomoto, and I. Hachisu, Astrophys. J. **595**, 1094 (2003).
[22] H. Saio and K. Nomoto, Astrophys. J. **615**, 444 (2004).
[23] S.-C. Yoon and N. Langer, Astron. Astrophys. **435**, 967 (2005).
[24] S.-C. Yoon, P. Podsiadlowski, and S. Rosswog, Mon. Not. R. Astron. Soc. **380**, 933 (2007).
[25] V. Kalogera, in *Compact Binary Mergers and Accretion-Induced Collapse: Event Rates*, edited by S. Meshkov, AIP Conf. Proc. 523 (AIP, New York, 2000).
[26] S. E. Woosley and E. Baron, Astrophys. J. **391**, 228 (1992).
[27] C. Fryer, W. Benz, M. Herant, and S. A. Colgate, Astrophys. J. **516**, 892 (1999).
[28] L. Dessart, A. Burrows, C. D. Ott, E. Livne, S.-Y. Yoon, and N. Langer, Astrophys. J. **644**, 1063 (2006).
[29] L. Dessart, A. Burrows, E. Livne, and C. D. Ott, Astrophys. J. **669**, 585 (2007).
[30] B. D. Metzger, A. L. Piro, E. Quataert, and T. A. Thompson, arXiv:0908.1127.
[31] L. R. Yungelson and M. Livio, Astrophys. J. **497**, 168 (1998).
[32] K. Belczynski, T. Bulik, and A. J. Ruiter, Astrophys. J. **629**, 915 (2005).
[33] Y.-Z. Qian and G. J. Wasserburg, Phys. Rep. **442**, 237 (2007).
[34] S. van den Bergh and G. A. Tammann, Annu. Rev. Astron. Astrophys. **29**, 363 (1991).
[35] P. Madau, M. della Valle, and N. Panagia, Mon. Not. R. Astron. Soc. **297**, L17 (1998).
[36] E. Scannapieco and L. Bildsten, Astrophys. J. Lett. **629**, L85 (2005).
[37] F. Mannucci, M. Della Valle, N. Panagia, E. Cappellaro, G. Cresci, R. Maiolino, A. Petrosian, and M. Turatto, Astron. Astrophys. **433**, 807 (2005).
[38] H. B. Perets, A. Gal-Yam, P. Mazzali, D. Arnett, D. Kagan, A. V. Filippenko, W. Li, S. B. Cenko, D. B. Fox, D. C. Leonard, D. Moon, D. J. Sand, A. M. Soderberg, R. J. Foley, M. Ganeshalingam, J. P. Anderson, P. A. James, E. O. Ofek, L. Bildsten, G. Nelemans, K. J. Shen, N. N. Weinberg, B. D. Metzger, A. L. Piro, E. Quataert, M. Kiewe, and D. Poznanski, arXiv:0906.2003.
[39] K. S. Kawabata, K. Maeda, K. Nomoto, S. Taubenberger, M. Tanaka, T. Hattori, and K. Itagaki, arXiv:0906.2811.
[40] K. S. Thorne, in *300 Years of Gravitation*, edited by S. W. Hawking and W. Israel (Cambridge University Press, Cambridge, England, 1987).
[41] N. Andersson, Classical Quantum Gravity **20**, R105 (2003).
[42] C. D. Ott, Classical Quantum Gravity **26**, 063 001 (2009).
[43] R. Mayle and J. R. Wilson, Astrophys. J. **334**, 909 (1988).
[44] E. Baron, J. Cooperstein, S. Kahana, and K. Nomoto, Astrophys. J. **320**, 304 (1987).
[45] F. S. Kitaura, H.-T. Janka, and W. Hillebrandt, Astron. Astrophys. **450**, 345 (2006).
[46] A. Burrows, L. Dessart, and E. Livne, in *The Multi-Dimensional Character and Mechanisms of Core-Collapse Supernovae*, edited by S. Immler and R. McCray, AIP Conf. Proc. No. 937 (AIP, New York, 2007).
[47] H. A. Bethe and J. R. Wilson, Astrophys. J. **295**, 14 (1985).
[48] A. Arcones, H.-T. Janka, and L. Scheck, Astron. Astrophys. **467**, 1227 (2007).
[49] B. D. Metzger, A. L. Piro, and E. Quataert, Mon. Not. R. Astron. Soc. **396**, 1659 (2009).
[50] H. Dimmelmeier, C. D. Ott, A. Marek, and H.-T. Janka, Phys. Rev. D **78**, 064056 (2008).
[51] A. Heger, S. E. Woosley, and H. C. Spruit, Astrophys. J. **626**, 350 (2005).
[52] S. E. Woosley and A. Heger, Astrophys. J. **637**, 914 (2006).
[53] C. D. Ott, A. Burrows, T. A. Thompson, E. Livne, and R. Walder, Astrophys. J. Suppl. Ser. **164**, 130 (2006).
[54] N. Stergioulas, Living Rev. Relativity **6**, 3 (2003).
[55] L. Baiotti, R. D. Pietri, G. M. Manca, and L. Rezzolla, Phys. Rev. D **75**, 044023 (2007).
[56] G. M. Manca, L. Baiotti, R. De Pietri, and L. Rezzolla, Classical Quantum Gravity **24**, S171 (2007).
[57] J. M. Centrella, K. C. B. New, L. L. Lowe, and J. D. Brown, Astrophys. J. Lett. **550**, L193 (2001).
[58] M. Shibata, S. Karino, and Y. Eriguchi, Mon. Not. R. Astron. Soc. **343**, 619 (2003).
[59] C. D. Ott, S. Ou, J. E. Tohline, and A. Burrows, Astrophys. J. **625**, L119 (2005).
[60] S. Ou and J. E. Tohline, Astrophys. J. **651**, 1068 (2006).
[61] C. D. Ott, Ph.D. thesis, Universität Potsdam, Potsdam, Germany, 2006, http://nbn-resolving.de/urn/resolver.pl?urn=urn:nbn:de:kobv:517-opus-12986.
[62] P. Cerdá-Durán, V. Quilis, and J. A. Font, Comput. Phys. Commun. **177**, 288 (2007).
[63] C. D. Ott, H. Dimmelmeier, A. Marek, H.-T. Janka, I. Hawke, B. Zink, and E. Schnetter, Phys. Rev. Lett. **98**, 261101 (2007).

[64] C. D. Ott, H. Dimmelmeier, A. Marek, H.-T. Janka, B. Zink, I. Hawke, and E. Schnetter, Classical Quantum Gravity **24**, S139 (2007).
[65] S. Scheidegger, T. Fischer, S. C. Whitehouse, and M. Liebendörfer, Astron. Astrophys. **490**, 231 (2008).
[66] A. L. Watts, N. Andersson, and D. I. Jones, Astrophys. J. Lett. **618**, L37 (2005).
[67] M. Saijo and S. Yoshida, Mon. Not. R. Astron. Soc. **368**, 1429 (2006).
[68] M. Cantiello, S.-C. Yoon, N. Langer, and M. Livio, Astron. Astrophys. **465**, L29 (2007).
[69] L. Piersanti, S. Gagliardi, I. J. Iben, and A. Tornambé, Astrophys. J. **598**, 1229 (2003).
[70] Y. T. Liu and L. Lindblom, Mon. Not. R. Astron. Soc. **324**, 1063 (2001).
[71] Y. T. Liu, Phys. Rev. D **65**, 124003 (2002).
[72] C. L. Fryer, D. E. Holz, and S. A. Hughes, Astrophys. J. **565**, 430 (2002).
[73] E. Livne, Astrophys. J. **412**, 634 (1993).
[74] E. Livne, L. Dessart, A. Burrows, and C. A. Meakin, Astrophys. J. Suppl. Ser. **170**, 187 (2007).
[75] A. Burrows, E. Livne, L. Dessart, C. D. Ott, and J. Murphy, Astrophys. J. **655**, 416 (2007).
[76] T. Zwerger and E. Müller, Astron. Astrophys. **320**, 209 (1997).
[77] M. Liebendörfer, Astrophys. J. **633**, 1042 (2005).
[78] H. Dimmelmeier, J. A. Font, and E. Müller, Astron. Astrophys. **388**, 917 (2002).
[79] H. Dimmelmeier, C. D. Ott, H.-T. Janka, A. Marek, and E. Müller, Phys. Rev. Lett. **98**, 251101 (2007).
[80] H. Dimmelmeier, J. Novak, J. A. Font, J. M. Ibáñez, and E. Müller, Phys. Rev. D **71**, 064023 (2005).
[81] M. Obergaulinger, M. A. Aloy, and E. Müller, Astron. Astrophys. **450**, 1107 (2006).
[82] A. Burrows, L. Dessart, E. Livne, C. D. Ott, and J. Murphy, Astrophys. J. **664**, 416 (2007).
[83] H. Dimmelmeier, J. A. Font, and E. Müller, Astron. Astrophys. **393**, 523 (2002).
[84] J. A. Isenberg, Int. J. Mod. Phys. D **17**, 265 (2008).
[85] P. Cerdá-Durán, G. Faye, H. Dimmelmeier, J. A. Font, J. M. Ibáñez, E. Müller, and G. Schäfer, Astron. Astrophys. **439**, 1033 (2005).
[86] Isabel Cordero-Carrion *et al.*, Phys. Rev. D **79**, 024017 (2009).
[87] B. Einfeldt, SIAM J. Numer. Anal. **25**, 294 (1988).
[88] H. Shen, H. Toki, K. Oyamatsu, and K. Sumiyoshi, Nucl. Phys. **A637**, 435 (1998).
[89] H. Shen, H. Toki, K. Oyamatsu, and K. Sumiyoshi, Prog. Theor. Phys. **100**, 1013 (1998).
[90] A. Marek, H.-T. Janka, R. Buras, M. Liebendörfer, and M. Rampp, Astron. Astrophys. **443**, 201 (2005).
[91] T. A. Thompson, A. Burrows, and P. A. Pinto, Astrophys. J. **592**, 434 (2003).
[92] A. Burrows, S. Reddy, and T. A. Thompson, Nucl. Phys. **A777**, 356 (2006).
[93] K. Langanke and G. Martinez-Pinedo, Nucl. Phys. **A673**, 481 (2000).
[94] R. Buras, M. Rampp, H.-T. Janka, and K. Kifonidis, Astron. Astrophys. **447**, 1049 (2006).
[95] http://www.stellarcollapse.org/AIC. AIC $Y_e(\rho)$ data.
[96] J. P. Ostriker and J. W.-K. Mark, Astrophys. J. **151**, 1075 (1968).
[97] I. Hachisu, Astrophys. J. Suppl. Ser. **61**, 479 (1986).
[98] H. Komatsu, Y. Eriguchi, and I. Hachisu, Mon. Not. R. Astron. Soc. **237**, 355 (1989).
[99] J.-L. Tassoul, *Stellar Rotation* (Cambridge University Press, Cambridge, England, 2000).
[100] S. I. Blinnikov, N. V. Dunina-Barkovskaya, and D. K. Nadyozhin, Astrophys. J. Suppl. Ser. **106**, 171 (1996).
[101] J. Pedlosky, *Geophysical Fluid Dynamics* (Springer, New York, USA, 1987).
[102] A. Piro, Astrophys. J. **679**, 616 (2008).
[103] B. Müller, Ph.D. thesis, Technische Universität München, München, Germany, 2009.
[104] M. Shibata and Y.-I. Sekiguchi, Phys. Rev. D **68**, 104020 (2003).
[105] K. S. Thorne, Rev. Mod. Phys. **52**, 299 (1980).
[106] A. Nagar, O. Zanotti, J. A. Font, and L. Rezzolla, Phys. Rev. D **75**, 044016 (2007).
[107] L. Baiotti, S. Bernuzzi, G. Corvino, R. de Pietri, and A. Nagar, Phys. Rev. D **79**, 024002 (2009).
[108] C. D. Ott, A. Burrows, E. Livne, and R. Walder, Astrophys. J. **600**, 834 (2004).
[109] R. Mönchmeyer, G. Schäfer, E. Müller, and R. Kates, Astron. Astrophys. **246**, 417 (1991).
[110] P. Goldreich and S. V. Weber, Astrophys. J. **238**, 991 (1980).
[111] A. Yahil, Astrophys. J. **265**, 1047 (1983).
[112] K. A. Van Riper, Astrophys. J. **257**, 793 (1982).
[113] R. Kippenhahn and A. Weigert, *Stellar Structure and Evolution* (Springer, Berlin, Germany, 1990).
[114] A. Burrows and J. M. Lattimer, Astrophys. J. **270**, 735 (1983).
[115] M. Liebendörfer, M. Rampp, H. Th. Janka, and A. Mezzacappa, Astrophys. J. **620**, 840 (2005).
[116] R. Buras, H.-T. Janka, M. Rampp, and K. Kifonidis, Astron. Astrophys. **457**, 281 (2006).
[117] K. Sumiyoshi, S. Yamada, H. Suzuki, H. Shen, S. Chiba, and H. Toki, Astrophys. J. **629**, 922 (2005).
[118] S. W. Bruenn, Astrophys. J. Suppl. Ser. **58**, 771 (1985).
[119] J. E. Tohline, Astrophys. J. **285**, 721 (1984).
[120] S. Rosswog, D. Kasen, J. Guillochon, and E. Ramirez-Ruiz, Astrophys. J. **705**, L128 (2009).
[121] E. Müller, M. Rampp, R. Buras, H.-T. Janka, and D. H. Shoemaker, Astrophys. J. **603**, 221 (2004).
[122] C. D. Ott, A. Burrows, L. Dessart, and E. Livne, Astrophys. J. **685**, 1069 (2008).
[123] http://www.stellarcollapse.org/gwcatalog. Gravitational Waveform Catalog at stellarcollapse.org.
[124] H. Dimmelmeier, N. Stergioulas, and J. A. Font, Mon. Not. R. Astron. Soc. **368**, 1609 (2006).
[125] http://www.mpa-garching.mpg.de/rel_hydro/wave_catalog.shtml. MPA-Garching GW Signal Catalog.
[126] http://ligo.caltech.edu. LIGO.
[127] http://www.et-gw.eu. Einstein telescope.
[128] S. A. Balbus and J. F. Hawley, Astrophys. J. **376**, 214 (1991).
[129] P. Cerdá-Durán, J. A. Font, and H. Dimmelmeier, Astron. Astrophys. **474**, 169 (2007).
[130] M. Saijo and S. Yoshida, Mon. Not. R. Astron. Soc. **368**, 1429 (2006).
[131] M. Saijo and Y. Kojima, Phys. Rev. D **77**, 063002 (2008).